This is a preprint, the final version is subject to change, of the American Mineralogist (MSA)
Cite as Authors (Year) Title. American Mineralogist, in press.
(DOI will not work until issue is live.) DOI: http://dx.doi.org/10.2138/am-2015-4847

The whole-block approach to measuring hydrogen diffusivity in nominally anhydrous minerals

Elizabeth Ferriss, Terry Plank, David Walker, and Meredith Nettles

Lamont-Doherty Earth Observatory, Columbia University, 61 Route 9W, Palisades, NY 10964

Abstract

A method is developed for determining the diffusivity of infrared-active species by transmission Fourier transform infrared spectroscopy (FTIR) in samples prepared as rectangular prisms *without* cutting the sample. The primary application of this "whole-block" or "3D-WB" method is in measuring the diffusion of hydrogen (colloquially referred to as "water") in nominally anhydrous minerals, but the approach is applicable to any IR-active species. The whole-block method requires developing a 3-dimensional model that includes the integration of the beam signal through the sample, from rim to core to opposite rim. The analysis is carried out using both forward and tomographic inverse modeling techniques. Measurements collected from central slices cut from the whole block are simpler to interpret than whole-block measurements, but slicing requires destructive sample analysis. Because the whole-block method is nondestructive, this approach allows a time-series of diffusion experiments on the same sample.

The potential pitfalls of evaluating whole-block measurements without correcting for path integration effects are explored using simulations. The simulations demonstrate that diffusivities determined from whole-block measurements without considering path-averaging may be up to half an order of magnitude too fast. The largest errors are in fast and/or short directions, in which

This is a preprint, the final version is subject to change, of the American Mineralogist (MSA)
Cite as Authors (Year) Title. American Mineralogist, in press.
(DOI will not work until issue is live.) DOI: http://dx.doi.org/10.2138/am-2015-4847

the diffusion profiles are best developed. A key characteristic of whole-block measurements is that the central values in whole-block traverses always change before the concentration of the IR-active species changes in the block's center because of signal integration that includes concentrations in the sample rims. The resulting plateau in the measurements is difficult to fit correctly without considering path integration effects, ideally by using 3D whole-block models. However, for early stages of diffusion with less than 50% progress, diffusivities can be accurately determined within 0.5 log units using a 1D approximation and the whole-block central plateau values because diffusivities are more dependent on profile shape than absolute concentrations.

To test the whole-block method, a dehydration experiment was performed on an oriented piece of diopside from the Kunlun Mts with minimal zoning, cracks, or inclusions. The experiment was performed in a gas mixing furnace for 3 days at a temperature of 1000 °C and oxygen fugacity of $10^{-11.1}$ bar (QFM). First, whole-block analysis was performed by taking FTIR traverses in three orthogonal directions. Then, a slice was cut from the center of the sample, and hydrogen profiles were measured by FTIR and secondary ion mass spectrometry (SIMS). The results of FTIR and SIMS measurements on the slice are in good agreement both with each other and with diffusion profiles calculated based on the results of forward and inverse models of the whole-block FTIR measurements. Finally, the new method is applied to previous whole-block measurements of hydrogen diffusion in San Carlos olivine using both the forward and inverse approaches.

This is a preprint, the final version is subject to change, of the American Mineralogist (MSA)
Cite as Authors (Year) Title. American Mineralogist, in press.
(DOI will not work until issue is live.) DOI: http://dx.doi.org/10.2138/am-2015-4847

Keywords

Transmission FTIR, diffusion, hydrogen, water in nominally anhydrous minerals, diopside, olivine

Introduction

Diffusion is an important transport mechanism and has numerous applications to the geological sciences (e.g., Watson and Baxter 2007). The mechanisms and rates of diffusion for many chemical species in geologically relevant systems are known (e.g., Zhang and Cherniak 2010), but diffusivities, also called diffusion coefficients, are still poorly constrained for many systems. Determination of the relatively slow diffusivities in crystalline materials has been tackled with a variety of techniques (Ryerson 1987), some of which are still emerging (Watson and Dohmen 2010). All of these methods require both an experimental approach that results in diffusion and a way to measure the extent of that diffusion.

Experimental methods may be divided into two broad categories: time-series or mass-loss experiments, which measure changes in concentration with time at a particular point, usually the center, of the sample, and diffusion profile experiments, which measure changes in concentration with distance at a given time. Sample geometry is a key factor in all diffusion experiments and is usually chosen in a way that simplifies the final diffusion analysis from Fick's 2nd Law, $\frac{\partial v}{\partial t} = D\frac{\partial^2 v}{\partial x^2}$, where D is the diffusivity, v is the concentration, t is the time, and x is the distance. Solutions are available for many geometries and boundary conditions in Carslaw and Jaeger 1959 and Crank 1975.

This is a preprint, the final version is subject to change, of the American Mineralogist (MSA)
Cite as Authors (Year) Title. American Mineralogist, in press.
(DOI will not work until issue is live.) DOI: http://dx.doi.org/10.2138/am-2015-4847 10/7

Experiments that are designed to measure diffusion profiles have the significant advantage that they can be directly compared to profiles calculated from the solution to Fick's 2nd Law, and transport that is unrelated to diffusion is readily apparent (Ryerson 1987). Time series experiments are, however, still useful to obtain an initial approximation for diffusivity and as a complimentary technique for confirming interpretations based on diffusion profile measurements (e.g., Woods et al. 2000). Other approaches useful for validation of diffusivity estimates include cross-checking with multiple experimental methods, varying the sample geometry, and zero-time experiments, in which the sample is removed from the experiment immediately after run conditions are achieved (Hofmann 1980). Although diffusion profiles are preferable to time-series measurements, profiles are more difficult to obtain because they traditionally require that the sample be cut through the middle after the experiment, which requires careful manipulation to avoid sample fracture or loss and also prevents the sample from being re-used in future diffusion experiments, e.g., to generate time-series measurements or perform a reversal.

Hydrogen (H^+; colloquially often referred to as "water") diffusivities in nominally anhydrous minerals (NAMs) are most often determined using measurements from transmission Fourier-transform infrared spectroscopy (FTIR) because this method is non-destructive, commonly available, inexpensive, more sensitive to hydrogen (> ppm level) than most other techniques, and can provide some structure and speciation information (see review by Rossman 2006). Reflectance FTIR may also be used to measure hydrogen and carbon speciation and concentration in glasses, but the detection limits for this method are generally too high (~1000 ppm wt. H_2O) for measuring hydrogen or carbon in nominally anhydrous minerals (Grzechnik et al. 1996; Hervig et al. 2003; King and Larsen 2013; Lowenstern and Pitcher 2013). Experimental methods and measurement techniques for hydrogen diffusion experiments in NAMs are

This is a preprint, the final version is subject to change, of the American Mineralogist (MSA)
Cite as Authors (Year) Title. American Mineralogist, in press.
(DOI will not work until issue is live.) DOI: http://dx.doi.org/10.2138/am-2015-4847

reviewed by Ingrin and Blanchard 2006 and Farver 2010. In the standard approach, a slice is cut from the center of a sample prior to diffusion profile measurements to minimize the effect of profile overlap (also called signal accumulation or integration) along a transmission path (Movie 1). By cutting, profile overlap effects are eliminated if the hydrogen has not diffused into the center of the slice and is of constant concentration in the thickness direction of the slice. Non-constant slice profiles can still be evaluated, but non-path-integrated three dimensional models must be used instead of relatively simple one dimensional models; see description below.

This paper describes how to acquire and interpret diffusion profile measurements for species measured by transmission FTIR without cutting the sample after a diffusion experiment (Figure 1). This approach, which we refer to as the whole-block method, takes advantage of the fact that the measured transmission FTIR concentration, normalized to thickness, represents a path-averaged value in the sample. We focus on hydrogen in nominally anhydrous minerals cut in the form of a rectangular parallelepiped, but other systems measured using a transmitted signal moderated by absorption such as carbon by FTIR or a heavy element by X-rays, and other sample geometries could also be evaluated using this approach. We explore this method using simulated data, test it experimentally by dehydrating diopside, and then apply it to published measurements on the hydration of olivine.

The whole-block approach

Signal accumulation in FTIR measurements provides an opportunity to obtain diffusion profiles without cutting the sample, which typically is a rectangular parallepiped oriented with respect to crystallographic or morphologic axes of the material. These profiles (Figure 1) will be called “whole-block” here to distinguish them from “slice” profiles measured on the central slice

This is a preprint, the final version is subject to change, of the American Mineralogist (MSA)
Cite as Authors (Year) Title. American Mineralogist, in press.
(DOI will not work until issue is live.) DOI: http://dx.doi.org/10.2138/am-2015-4847

of a sample cut after the diffusion anneal. In this section we describe the advantages of using whole-block measurements as well as the details of the method. The whole-block method involves (1) measurements of hydrogen concentration profiles through the entire, uncut sample block, (2) forward modeling to obtain diffusivity estimates, and (3) inversion of the whole-block measurements to provide an independent determination of the internal concentration structure of the sample.

Advantages

Whole-block measurements are useful for the following reasons: (1) whole-block measurements can be obtained nondestructively and thus permit multiple experiments using the same sample, e.g., a time series of progressively longer experiments or reversal of diffusion flux by change of external reservoir concentration to promote diffusion into or out of a specimen. (2) The cut slice may be too thin to provide a high quality FTIR signal for samples with low, ppm-level hydrogen concentrations. (3) The diffusivities in three orthogonal directions can be estimated from the same sample. Measurements for the third direction otherwise requires either a second experiment or a slice taken from one of the butts left from the original slice. (4) In dehydration experiments, the initial profile can be measured directly. (In hydration experiments on pre-annealed samples, the initial concentration is 0 everywhere.)

The whole-block method also allows some independence from the following problems that can sometimes result in high error in measurements taken near the edge of sample slices. The rim hydrogen concentration may be very low after a dehydration experiment, which causes high errors in FTIR calibrations. Rims are also less likely to be perfectly flat than the center of a polished block because of chipping during cutting and/or polishing and/or quenching. If the

This is a preprint, the final version is subject to change, of the American Mineralogist (MSA)
Cite as Authors (Year) Title. American Mineralogist, in press.
(DOI will not work until issue is live.) DOI: http://dx.doi.org/10.2138/am-2015-4847

sample block shape is wedged and does not have near-perfect 90° angles, then the FTIR beam does not sample the full thickness at some rims, resulting in artificially low values. Further, in some thicker samples, scattering of the infrared beam near edges and cracks may result in artificially low values.

Whole-block measurements taken in the center of the sample always show an apparent decrease for dehydration experiments or increase for hydration in hydrogen content in the center of a whole-block profile (see discussion and illustrations below) and therefore provide diffusion information in the ray path direction without the problems associated with rim measurements. While whole-block measurements also include rim effects, the central values, which include integrated values from the rims, provide additional measurements to improve the overall interpretation. Because the whole-block method is non-destructive, the sample can always be sliced to confirm the final interpretation and resolve any ambiguity.

Whole-block profile measurements

Whole-block concentration measurements are constructed by normalizing the peak area of the FTIR absorbance spectra of interest obtained after the experiment to the maximum hydrogen concentration, which is the initial concentration for diffusion out of the sample or the solubility for diffusion into the sample. The relevant OH vibrations occur between wavenumbers 3000 and 4000 cm^{-1}. The resulting area ratios can be used directly in subsequent forward and inverse analyses, or these values can be scaled up to the maximum hydrogen concentration and expressed in concentration units such as ppm wt. H_2O or $H/10^6$ Si.

Diffusion studies have somewhat more leeway in how FTIR spectra are evaluated than studies concerned with absolute hydrogen concentrations because the diffusivity estimate

This is a preprint, the final version is subject to change, of the American Mineralogist (MSA)
Cite as Authors (Year) Title. American Mineralogist, in press.
(DOI will not work until issue is live.) DOI: http://dx.doi.org/10.2138/am-2015-4847

depends on the overall shape, not the absolute values, of the concentration profiles. Thus, approaches likely to introduce errors in absolute concentration values are often permissible as long as they are applied uniformly to all spectra in the profile. For instance, linear baselines are unusual in concentration studies but common in diffusion studies because they provide consistency among measurements both along the profile and before and after the experiment (e.g., Ingrin et al. 1995). The resulting concentration profiles may not be entirely accurate in their absolute concentrations, but they still provide good estimates of the diffusivities, even after diffusion has reached the center of the sample, in which case a 3-dimensional model such as one described below is required.

Also unlike concentration studies, either polarized or unpolarized infrared radiation may be used, even in highly birefringent or anisotropic samples. In the case of unpolarized radiation, which can be slightly polarized due to prisms and mirrors along its optical path, the absorbance spectrum changes with ray path R, which is also called the propagation direction or thickness direction. Polarized radiation has the advantages of providing more meaningful additional structural and concentration information and allowing consistent spectra between profiles if the electric vector E is maintained in a constant direction, ideally the direction with the strongest absorbance. However, unpolarized radiation typically has a higher signal-to-noise ratio and may be necessary in samples with very low concentrations. Woods et al. (2000) measured hydrogen diffusion profiles in diopside using both polarized and unpolarized radiation and obtained the same diffusivity within error.

Forward modeling to obtain diffusivities requires whole-block profiles (Figure 1) measured parallel to three orthogonal directions. The simplest geometry for obtaining these profiles is a centered cross of measurements using one infrared ray path and a line of measurements through

This is a preprint, the final version is subject to change, of the American Mineralogist (MSA)
Cite as Authors (Year) Title. American Mineralogist, in press.
(DOI will not work until issue is live.) DOI: http://dx.doi.org/10.2138/am-2015-4847 10/7

the center of the sample using a second ray path. Profiles obtained using three separate ray paths, additional off-center profiles, and/or full concentration maps are not necessary to produce diffusivity estimates but would contribute to and support the final analysis, particularly for the inverse approach described below.

Forward models

Whole-block profiles (3D-WB)

Whole-block profiles can be calculated from a 3-dimensional (3D) array of hydrogen concentrations determined from standard three-dimensional models (given below) by taking the arithmetic mean of the concentrations in the direction parallel to the infrared beam ray path (R) for each measurement. For example, for a whole-block point (x,y) measured with R // [100], the whole-block (3D-WB) concentration $v_{3D\text{-}WB}$ equals the average of all concentration points along [100] at (x,y). Unlike slice profiles, whole-block profiles can often be conveniently obtained with R parallel to two different directions, e.g., a traverse // [100] with R // [010] and a traverse // [100] with R // [001]. Because they represent averages, these two profiles may differ significantly, particularly when diffusion is strongly anisotropic.

This averaging must take place in the absorbance A domain, which is linearly related to the concentration v according to the Beer-Lambert law (A = v × molar absorption coefficient ε × thickness), rather than in the transmission domain. In FTIR, the transmission T is the variable that is actually measured, and $T = I / I_0$ where I is the intensity of measured light and I_0 initial intensity. The absorbance $A = -\log_{10}T$; although other log scales may also be used with an appropriate conversion factor for ε when calculating v from A. The absorbance is conventionally reported by most commercial software for FTIR spectrometers. For each unit step through the

sample, the intensity is changed by a percentage of the initial value entering that unit, resulting in an exponential change in the transmission.

The concentration of the diffusing species being measured, and hence the extent of that exponential change, varies along each unit step-size in the integrated whole-block path after a diffusion experiment. To understand the mathematics involved, consider the simplified example of a zoned sample with three distinct parts, in which each part has a different concentration of the IR-active species and hence different transmittances. The IR radiation first passes through Part 1 to produce transmittance $T_1=I_1/I_0$, then passes through Part 2 to produce transmittance $T_2=I_2/I_1$, and finally through Part 3 to produce $T_3=I_3/I_2$. The generic sample in this example does not have to be symmetric, although a symmetrical diffusion profile is assumed in the whole-block diffusion forward models. The final transmittance, $T_{total} = T_1 \times T_2 \times T_3 = I_3/I_0$. (Following this equation, whole-block path-integrated values may be calculated in the transmission domain by using the product, not the average, of transmittance values along the ray path.) Because A is related to T on a log scale (A=-log$T$), the total absorbance A_{total} is determined from the component A values as a sum rather than a product: A_{total}= -log(T_{total}) = -log($T_1 \times T_2 \times T_3$) = -log$T_1$ + -logT_2 + -logT_3 = $A_1 + A_2 + A_3$. For a system with n concentration zones, $A_{total} = \sum_{i=1}^{n} A_i$. Therefore, the integrated absorbance or concentration divided by the sample thickness represents the arithmetic mean of absorbance or concentration values in the ray path of the measurement, assuming that the grid size used to calculate the profile is evenly spaced and sufficiently fine-scale that the concentration in each division is approximately uniform.

This is a preprint, the final version is subject to change, of the American Mineralogist (MSA)
Cite as Authors (Year) Title. American Mineralogist, in press.
(DOI will not work until issue is live.) DOI: http://dx.doi.org/10.2138/am-2015-4847

3D non-path-integrated (3D-NPI) and 1D diffusion

Production of the 3D-WB profiles described above assumes some knowledge of the internal concentration structure of the sample, which can be determined using standard 3-dimensional models for diffusion in a rectangular parallelepiped such as those found in Carslaw and Jaeger (1959) Section 6.4, Crank (1975) Section 2.5.1, and Demouchy et al. (2006). These models are based on either infinite sums of sines and cosines or error functions. In general, error functions are preferred for the early stages of diffusion, and the infinite sum more accurately represents diffusion at later stages (Crank 1975, Section 2.1). All models discussed here assume that the diffusivity is independent of the concentration of the diffusing species. This assumption may not hold for hydrogen diffusion in all NAMs (e.g., mantle-derived pyrope, Wang et al. 1996) and is certainly incorrect for silicate glasses (e.g., Doremus 1975; Lanford et al. 1979; Zhang et al. 1991, Anovitz et al., 1999).

Examples for several boundary conditions are written out in Carslaw and Jaeger (1959) section 6.4 for diffusion in an isotropic rectangular parallelepiped. Carslaw and Jaeger (1959) further note that the same approach (i.e., the multiplication of known one-dimensional problems, with a proof given in their Section 1.15) is also applicable to anisotropic media, given the critical assumption that the main axes of diffusion are parallel to the coordinate planes of the parallelepiped. For instance, for the region $L_a > x > 0$, $L_b > y > 0$, $L_c > z > 0$ with unit initial concentration and zero surface concentration, the concentration at all positions in the crystal $v(x,y,z)$ is as follows:

$$v(x,y,z) = erf\left(\frac{x}{2\sqrt{D_a t}} + \text{erf}\left(\frac{L_a - x}{2\sqrt{D_a t}}\right)\right) erf\left(\frac{y}{2\sqrt{D_b t}} + \text{erf}\left(\frac{L_b - y}{2\sqrt{D_b t}}\right)\right) erf\left(\frac{z}{2\sqrt{D_c t}} + \text{erf}\left(\frac{L_c - z}{2\sqrt{D_c t}}\right)\right) \quad \text{Eq. 1}$$

where t is time and D_a, D_b, D_c are the diffusivities parallel to each direction. Throughout this manuscript, we refer to this model as three-dimensional non-path-integrated (3D-NPI).

For individual non-path-integrated concentration profiles (e.g., slice profile measurements along a single dimension) in which the concentration of the diffusing species in the center of the sample remains constant throughout the experiment, then the diffusivity can be determined more simply using a 1-dimensional (1D) model, e.g.,

$$v(x)_{1D} = \left(\text{erf}\left(\frac{x}{2\sqrt{D_a t}}\right) + \text{erf}\left(\frac{L_a - x}{2\sqrt{D_a t}}\right)\right). \quad \text{Eq. 2}$$

Inverse models: Geochemical tomography

Inversions similar to those used to evaluate geophysical tomography data constitute a complementary analysis technique to the forward models described above. While inverse models cannot by themselves provide diffusivity estimates, they produce independent estimates of the internal concentration structure that provide a useful constraint and check on the concentration profiles and true center concentration values predicted by forward models. Unlike forward models, inverse models require no assumptions about diffusion or any concentration changes over the course of the experiment. The data d constraining our model are the whole-block estimates of path-averaged concentrations obtained as described above. As in all inverse modeling, errors in the observations arising from the measurement technique and assumptions

will lead to some level of uncertainty in the final model. For example, in our case we assume that our sample is a single crystal with uniform mineral composition to produce integrated concentration estimates from FTIR.

A more complete treatment of discrete inverse theory and examples for geophysical data may be found in Menke (1984). Here we include only a brief overview of the technique. The sample, a rectangular prism, is subdivided into a series of regularly spaced miniature prisms or blocks of equal volume, and each of these sub-blocks is assumed to have uniform concentration. Each whole-block observation represents the average concentration through a subset of these blocks. The problem is then formulated as the equation $G \cdot m = d^{obs}$, where d^{obs} is an $n \times 1$ matrix containing n whole-block observations, m is a $k \times 1$ coefficient matrix containing k concentration values (1 for each subdivision of the sample; these are the values we solve for), and G is an $n \times k$ sensitivity matrix that describes the contribution of each of the k sample subdivisions to the whole-block measurements d^{obs}. The grid spacing, which determines k, is varied in each direction with the goal of describing the measurements as simply as possible, i.e., with a smallest value of k that adequately describes the measurements.

The internal concentration values are determined by minimizing a goodness of fit measure related to the variance $\sigma^2 = \frac{\sum(d^{obs} - d^{pred})^2}{\overline{d^{obs}}^2}\left(\frac{1}{k}\right)$, where d^{pred} represents the whole-block values predicted from the model results, k is number of degrees of freedom (i.e., the number of grid cells used to model the measurements), and $\overline{d^{obs}}$ is the mean of the observed measurements, which serves as a scaling factor to compare the goodness of fit between data sets. The error σ_i on each concentration value i is evaluated as $\sigma_i = \overline{d^{obs}}\sqrt{C(i,i)}$, where C is the covariance matrix $C = [G^T G] \cdot \sigma^2$, and G^T is the transpose of G. The formal error σ_i on each value is a minimum value

because it only includes the diagonal elements of the covariance matrix. To better assess the true error, comparable whole-block data can be simulated and then inverted using the same approach as that used to invert the measurements of interest.

Ideally, whole-block profiles would be obtained with at least three lines measured along three different orthogonal planes of the sample block as well as additional, off-center profiles. Newer FTIR spectrometers are equipped with digital stages and software that can rapidly produce hydrogen measurement maps of entire surfaces with consequent improvement in the accuracy of internal concentrations determined from the inversion. However, many laboratories will be limited to the bare minimum required to apply the whole-block forward models: a cross of measurements with one ray path and a single line of measurements with a different ray path.

A successful inversion is possible with a limited set of analyses by applying model constraints to the rim values, symmetry, and/or smoothness of the model, following standard practice in geophysical tomography. A rim value constraint encourages the model to match the concentration in the subdivisions along the outermost rim of the sample to a known value. A symmetry constraint gives preference to model outputs that are symmetrical along any orthogonal line through the sample. A smoothness constraint causes the model to expect that neighboring subdivisions contain similar values. Damping the model output through the application of these constraints does not force the results (m) to comply exactly with the constraints, and a weighting factor λ can be included and varied to evaluate the importance of these constraints during the calculation. Each of the three constraints can be removed or weighted separately to evaluate their effects on the fit individually. The value of λ should be kept as low as possible so that the results are influenced primarily by the observed measurements.

This is a preprint, the final version is subject to change, of the American Mineralogist (MSA)
Cite as Authors (Year) Title. American Mineralogist, in press.
(DOI will not work until issue is live.) DOI: http://dx.doi.org/10.2138/am-2015-4847

Methods

Simulations were performed to provide more general insight into the potential for error when applying 3D-NPI and 1D diffusion models to path integrated measurements. Then, the whole-block approach was tested experimentally by dehydrating a diopside crystal and comparing the resulting whole-block profiles with slice profiles. In the final section, we review previously published whole-block profiles on hydrogen diffusion in olivine.

Numerical simulations

To investigate the usefulness and potential pitfalls of applying non-path-integrated diffusion models to path-integrated measurements, 40,000 sets of 3D-WB data were simulated and then fit using NPI models. In each simulation, 100 data points were generated along each of three orthogonal whole-block profiles. Then, NPI profiles were fit to these simulated 3D-WB data using the non-linear least squares fitting routine available in MATLAB curve-fitting toolbox. This least squares method is objective but somewhat biased toward fitting points closer to the sample rim where the points and the fit line can show the largest deviations from each other.

Simulations were performed assuming diffusion into the sample for isotropic and anisotropic materials, equant and inequant samples, and early to later stages of diffusion (up to 80% saturation, at which point the profiles are approaching a straight line, and error functions no longer produce good fits). Two different NPI fitting approaches were tested using different initial concentrations during the NPI fit: a 3D-NPI fit that uses the true, known initial value of zero, and a set of three 1D-NPI fits (one for each profile direction) that use the plateau in the 3D-WB data in place of the initial value during the fit.

This is a preprint, the final version is subject to change, of the American Mineralogist (MSA)
Cite as Authors (Year) Title. American Mineralogist, in press.
(DOI will not work until issue is live.) DOI: http://dx.doi.org/10.2138/am-2015-4847

Experiments

Sample preparation

A dehydrogenation experiment was performed on a diopside from the Kunlun Mountains, China, similar samples to which were used in previous diffusion experiments (Van Orman et al. 1998, 2001). The sample was prepared as a 3.5 mm × 1.6 mm × 1.8 mm orthogonal prism with faces perpendicular to [100]* (which is ~16° from [100]), [010], and [001], and polished using 1 μm diamond paste.

3D-WB measurements

Unpolarized FTIR measurements were obtained before and after the experiment using a spot size of 100 μm, resolution of 4 cm^{-1}, and averaged over 200 scans on the Nicolet 20 XSB with IR microscope at the American Museum of Natural History. To aid in FTIR spot location in the absence of a digital sample holder, pits were placed along each of the three orthogonal profiles in 100 μm intervals using a laser ablation microprobe. Initial integrated peak areas for unpolarized FTIR spectra with linear baselines range between 20 and 80 cm^{-2}, depending on the ray path direction. The precision error for the FTIR areas is 2%, based on repeated measurements at the same location according to the following equation: $100\times\sigma/(m\times\sqrt{n})$, where σ is a single standard deviation and m is the mean area for n=3 measurements.

Dehydration

The prepared sample block was heated in a gold-calibrated (error ± 3°) 1-atm vertical alumina tube furnace for 75 hours at 1000 °C and $10^{-11.1}$ bar oxygen fugacity (at the quartz-fayalite-magnetite buffer) using CO/CO_2 mixes of 97.0% CO_2 (Deines et al. 1974). The resulting absorbance values were normalized to the initial profile measurements to generate whole-block

This is a preprint, the final version is subject to change, of the American Mineralogist (MSA)
Cite as Authors (Year) Title. American Mineralogist, in press.
(DOI will not work until issue is live.) DOI: http://dx.doi.org/10.2138/am-2015-4847

342 diffusion profiles in three orthogonal directions with concentration units of final absorbance (A) /
343 initial absorbance (A_0). The precision error for A/A_0 concentration values of 3% was determined
344 by propagation of the 2% precision error on each measurement.

345 **Slice measurements by FTIR and SIMS**

346 After whole-block profiles were obtained, the sample was sliced perpendicular to [100]*,
347 and slice measurements were obtained parallel to [010] and [001] by unpolarized FTIR and
348 secondary ion mass spectrometry (SIMS). Concentrations profiles for the slice FTIR
349 measurements were generated by normalizing to the initial FTIR absorbance values adjusted for
350 thickness. One potential concern with this approach is that absorbance measurements obtained
351 using unpolarized radiation may not be directly proportional to thickness, at least for grains with
352 unpolarized absorbance greater than 0.15 and linear polarized absorbance greater than 0.3
353 (Libowitzky and Rossman 1996; Kovacs et al. 2008; Sambridge et al. 2008; Withers 2013; Xia et
354 al. 2013). All initial absorbance values used here are less than 0.13, and therefore should scale
355 directly with thickness.

356 SIMS measurements were carried out at the Carnegie Institution of Washington (DTM)
357 using the Cameca 6f ion microprobe. The primary beam of Cs^+ was 5-10 nA. The accelerating
358 voltage was 10 kV, and the final spot size was 20-40 μm. Hydrogen was measured as $^{16}O^1H$. The
359 ratio $^{16}O/^{30}Si$ was monitored, and concentrations were obtained following the procedures in
360 Wade et al. (2008). The SIMS measurements were calibrated using clinopyroxene standards
361 PMR-53, ROM271-10, -16 and -21. Standard concentrations are given in Aubaud et al. (2007).
362 The calibration factor for SIMS was 4540 ± 560 ppm wt. H_2O/(counts/s), which corresponds to
363 an accuracy or calibration error of 12%. The SIMS precision errors were determined similarly to

This is a preprint, the final version is subject to change, of the American Mineralogist (MSA)
Cite as Authors (Year) Title. American Mineralogist, in press.
(DOI will not work until issue is live.) DOI: http://dx.doi.org/10.2138/am-2015-4847

364 those for FTIR using n=4 to 5 measurements of each data point, and these errors ranged from 1.6
365 to 7.9 %.

366 **Initial concentration**

367 Initial concentration estimates through the untreated whole block of the Kunlun diopside
368 were complicated by the lack of an infrared polarizer on the FTIR at the time this work was
369 begun. An initial concentration of 33 ppm wt. H_2O was calculated from the average unpolarized
370 spectra measured along three orthogonal ray paths and using polynomial baselines with the
371 clinopyroxene calibration of Bell et al 1995. The error associated with estimating the total
372 absorbance in this way may be considerable but cannot be estimated accurately (Withers 2013).
373 Nonetheless, this value is nearly identical to the average of the eight SIMS measurements that
374 create a plateau of 34.3 +/- 0.6 ppm H_2O in the central slice of the heated whole block (shown in
375 Figure 5). When FTIR measurements are scaled to this SIMS value, they overlap in
376 concentrations, supporting both the initial FTIR estimate, and the initial value still preserved in
377 the core of the block. Thus to facilitate comparison with the SIMS measurements, the FTIR
378 concentrations were scaled up from A/A_0 to units of ppm wt. H_2O using a concentration of 34
379 ppm wt. H_2O.

380 **Forward models**

381 Diffusivities were determined from the whole-block diffusion profiles and each of the two
382 sets of slice profiles (FTIR and SIMS measurements) by least-square fits assuming a starting
383 concentration of 34 ppm wt. H_2O and an equilibrium concentration of 0 ppm and using both 3D-
384 WB and 3D-NPI approaches. Fits using 1D models are identical to 3D-NPI because diffusion has
385 not reached the center of the sample.

Inverse models

Inverse analysis of the 3D-WB measurements were performed for both the Kunlun diopside and previously published San Carlos olivine hydration measurements (Demouchy and Mackwell 2006) using comparable parameters, with the main focus on San Carlos olivine. The ray paths for the San Carlos olivine measurements are as follows: for the traverse // [100], *R* is // [010]; for the traverse // [010], *R* is // [100]; and for the traverse // [001], *R* is // [010] (Sylvie Demouchy, personal communication). To determine the best set of parameters, the number of grid cells in each direction was systematically increased, and λ was varied to minimize the variance while fitting the olivine profiles as simply as possible (Table 1). Preference was given to odd-numbered grid cell spacing to reduce ambiguity about which values in the central slices were sampled by observations. The maximum number of grid cells was restricted to 5 // [100], 11 // [010], and 9 // [001] to avoid including parameterized sections unconstrained by observations. Final grids were 9 × 9 × 9 in diopside and 5 × 9 × 9 for San Carlos olivine. A constraint weighting factor λ of 0.05 was applied for both smoothness and symmetry to both sets of measurements, and the rim value was not constrained for the diopside.

In addition to calculating the formal error σ_i, which is a minimum value, we assessed the true error on the inversion by simulating a comparable number and distribution of noise-free whole-block hydration profiles followed by inversions. The resulting calculated central value estimate was then compared to the known central value as a function of time and diffusivity // [100] to assess the error. For simplicity, the simulated profiles were produced using only a single-mechanism model of diffusion starting at 0 and increasing to a final solubility of 10 ppm wt. H_2O. The diffusivities // [010] and [001] were held constant at $10^{-13.4}$ and $10^{-12.2}$ m^2/s, and the diffusivity // [100] was varied from 10^{-11} to $10^{-12.5}$ m^2/s. Removing the rim value constraint while

This is a preprint, the final version is subject to change, of the American Mineralogist (MSA)
Cite as Authors (Year) Title. American Mineralogist, in press.
(DOI will not work until issue is live.) DOI: http://dx.doi.org/10.2138/am-2015-4847

409 retaining smoothness and symmetry constraints decreased the error in the simulated profile
410 inversions considerably, e.g., from 0.7 below the true value to near 0 ppm wt. H_2O error for
411 simulated profiles after 20 hours and $D_{// [100]}=10^{-12}$ m^2/s.

412 **Results and Discussion**

413 In the following sections, we first use numerical simulations to determine the errors that
414 might occur in calculated diffusivities if 3D-whole block (3D-WB) data are interpreted using a
415 3D-non-path-integrated (3D-NPI) model. We then verify both the forward and inverse 3D-WB
416 methods by obtaining both 3D-WB and slice data on a natural diopside sample that has been
417 dehydrated in the laboratory. Finally, we consider some pitfalls that may occur using published
418 3D-WB data for olivine diffusion.
419 There are three general issues at stake in interpreting 3D-WB data. One is the effect on
420 calculated diffusivities; another is the effect on calculated concentrations. These are separate
421 issues, and we demonstrate that it is possible to calculate accurate diffusivities from profile
422 shapes, without knowing absolute or even central value concentrations. The final issue is how
423 one interprets 3D-WB data in terms of equilibrium partitioning or solubility. Here accurate
424 determination of absolute concentrations from core to rim is essential.

425 ***Numerical simulations***

426 Simulation results are illustrated for 3D-NPI models used to fit simulated 3D-WB data in
427 Figure 2 and for the 1D-NPI models that use the plateau in place of the initial value in Figure 3.
428 The extent of diffusion progress with time is represented by percent saturation of the sample. The
429 absolute values of the errors in the best-fit diffusivity on a log scale were added together across
430 all three orthogonal directions to produce a single summed error for each simulation. The effect

This is a preprint, the final version is subject to change, of the American Mineralogist (MSA)
Cite as Authors (Year) Title. American Mineralogist, in press.
(DOI will not work until issue is live.) DOI: http://dx.doi.org/10.2138/am-2015-4847 10/7

of changing ray paths was also investigated for samples with varying levels of diffusive anisotropy. The results differ for individual directions, but the final summed errors are the same as in Figure 2 and Figure 3.

The diffusivities estimated using 3D-NPI applied to 3D-WB simulated data are generally too large, which corresponds to faster diffusion. This error is concentrated on well-developed profiles in fast or short directions and results in errors in both the absolute value of the diffusivity and the apparent anisotropy. This error arises primarily because the 3D-NPI fit requires at least one diffusion direction fast enough for diffusion to reach the center of the sample to account for relatively rapid changes in the central value of 3D-WB data.

Changes in the apparent central value

An important potential source of confusion when interpreting 3D-WB measurements comes from differences between the central values of 3D-WB data and those of slice data. The central value in a given whole-block profile always changes from the initial value before the concentration in the actual center of the sample changes because the central measurement includes the concentration at the rims (Movies 2 and 3; still image in Figure 4). If, for example, the diffusing species begins to diffuse into a sample block with initial concentration C_i=0 from all sides, then the average value of the concentration measured through the sample thickness in any given direction necessarily increases from 0. The whole-block profile will then show an apparent increase in concentration due to contributions from the sample rim in the FTIR integrated value, *but the concentration in the center of the sample may still be 0.*

During 3D-NPI analysis of slice measurements, the concentration measured at the center of each profile must be the same in all three directions because only one central point exists. In contrast, the central values measured in whole-block profiles, because they represent averages,

may differ for each of the six possible orientations: the profile // [100] with ray path *R* // [010]; // [100] with *R* // [010]; // [010] with *R* // [100]; // [010] with *R* // [001]; // [001] with *R* // [100]; and // [001] with *R* // [010]. This effect is more pronounced when *R* is parallel to a faster direction.

Effect of diffusion progress

The summed error for the 3D-NPI fit tends to first increase as the difference increases between the central values in the whole-block profiles, which change immediately, and the slice profiles, which remains constant at C_i=0 until the total concentration change in the sample reaches ~17% saturation. The error then decreases after diffusion reaches the center of the sample. After hydrogen reaches the center, the shape of the best-fit 3D-NPI profiles are able to match the 3D-WB simulated data much better than in previous stages of diffusion, resulting in improved fits (lower r^2 values) and lower summed error (e.g., Figure 2-A1 versus -A2). This improved fit likely results because once hydrogen has reached the center of the sample, the shape of all three orthogonal profiles for both slice and 3D-WB simulated data are controlled by diffusion only in the fast and/or short direction(s) from which hydrogen is infiltrating rather than in all three directions. After the center is reached, diffusivities in the long and/or slow-direction are usually modeled correctly (e.g., // [001] in Figure 2-A1 and -B1), and the error is entirely in the fast or short directions(s). That error in the fast or short direction also tends to decrease with diffusion progress as the system approaches saturation.

Effect of sample geometry and anisotropy

The effect of crystal shape was investigated by holding two sides of a rectangular parallelepiped sample constant at 2.2 mm and varying the length of the third side in a sample

This is a preprint, the final version is subject to change, of the American Mineralogist (MSA)
Cite as Authors (Year) Title. American Mineralogist, in press.
(DOI will not work until issue is live.) DOI: http://dx.doi.org/10.2138/am-2015-4847

with isotropic diffusion ($\log_{10}D$=-14 in m^2/s). The effect of changing anisotropy was investigated in the same way for an equant crystal (each side 2.2 mm) with diffusivities held constant at $\log_{10}D$=-14 m^2/s in two orthogonal directions and varied in the third direction (Figure 2B).

The 3D-NPI models typically provide the poorest fit and highest errors in short and/or fast direction(s), which have the most well developed profiles, whereas profiles parallel to slow and/or long directions, which are largely controlled by diffusion from other directions, are relatively easy to fit and do not significantly contribute to the overall error. Equant, isotropic samples have higher error than those with any deviation, perhaps because they lack any direction that is largely controlled by another and so have relatively high errors in all directions. In contrast, 3D-WB data with a single fast direction are modeled remarkably well with 3D-NPI models (right side of Figure 2B) likely because of this low error associated with long/slow directions and because the signal integration, which causes 3D-WB profiles to deviate from slice profiles, is minimized when the ray path is parallel to a slow direction.

In these simulations, the maximum summed error in the diffusivities is around 10% on a log scale. For diffusivities on the order of 10^{-14} m^2/s, 10% summed log error corresponds to estimated diffusivities in each direction that are about a factor of 5 too fast. This error is concentrated on the fast and short direction(s) of a rectangular parallelepiped, resulting in errors in the calculated extent of anisotropy, and is most pronounced when the concentration in the center of the sample first changes significantly from the initial concentration. These factor of 5 errors are associated with simulated, and therefore perfect, data. As shown in the next section, the error associated with fitting a 3D-NPI model to real 3D-WB measurements may be closer to a full order of magnitude.

This is a preprint, the final version is subject to change, of the American Mineralogist (MSA)
Cite as Authors (Year) Title. American Mineralogist, in press.
(DOI will not work until issue is live.) DOI: http://dx.doi.org/10.2138/am-2015-4847

A 1D approximation using central plateau values

If the goal is only to extract diffusivities, as opposed to true concentrations, it is possible to obtain better fits using NPI models than those shown Figure 2 by assuming that the central plateau in the 3D-WB data is also the initial value during fitting. This assumption is clearly not the case because the central concentration measured through the whole block is neither the initial nor the true center value, but a path integrated value. Nonetheless, by taking the measured 3D-WB central value as both the initial and final concentration, the fitting procedure becomes entirely dependent on the curvature of the profile, which has enough information to predict a diffusivity that is remarkably accurate, especially for early stages of diffusion. For diffusion progress less than 50%, the total summed error on the three diffusivities is less than 0.5 log units (Figure 3). As diffusion progresses and the shape of the profiles change to become less steep, the assumption of no change in the true central concentration (essentially the approximation here) becomes worse, and the corresponding fits also worsen. A set of three 1D profiles works better than 3D-NPI (which we explored but do not show here) for use in this approximation because it allows greater flexibility to accommodate differences in the 3D-WB profile plateau values (Figure 4). Moreover, with a 1D approximation, profiles are not needed in all three directions to provide a diffusivity estimate. Thus, while the full 3D-WB approach is certainly preferable for obtaining accurate diffusivities and concentrations, the 1D approximation using the central plateau values can provide a reasonable estimate of the diffusivities based on 3D-WB measurements. Interpretations that rely on an understanding of true concentrations, however, still require forward or inverse methods that take path integrations effects into account. Examples of such applications include partitioning, equilibrium solubility, and “metastable equilibrium”, a concept we discuss in the final section on hydrogen diffusion in olivine.

This is a preprint, the final version is subject to change, of the American Mineralogist (MSA)
Cite as Authors (Year) Title. American Mineralogist, in press.
(DOI will not work until issue is live.) DOI: http://dx.doi.org/10.2138/am-2015-4847

521 ***Experiments***

522 After the 3D-WB measurements were obtained for heat-treated Kunlun diopside by FTIR,
523 the central slice of the treated block was cut perpendicular to [100]* and analyzed by both FTIR
524 and SIMS. The resulting hydrogen concentration profiles are reported in Supplementary Table 1
525 and plotted in Figure 5. When the unpolarized A/A_o FTIR measurements are scaled to a 34 ppm
526 wt. H_2O initial value, the central slice zonation and central plateau are very similar to those
527 measured by SIMS, with concentrations overlapping within the analytical precision for many
528 points. Both the SIMS and FTIR measurements show a sudden drop of ~10 ppm wt. H_2O near
529 the center of the slice in the profile parallel to [001]. This drop suggests non-diffusive behavior
530 unrelated to measurement precision, although no nearby cracks were visible. The concentrations
531 measured through the treated whole block are lower than the intial value because of path
532 integration through the lower-concentration rims.

533 We applied the inverse tomographic method to these whole block measurements to solve for
534 the 3-D concentration structure using a $9 \times 9 \times 9$ grid and symmetry and smoothness constraints
535 with weighting parameter λ=0.05. The fit to the whole block data is shown Figure 6A, and the
536 predicted profiles in the central slices based on the inversion is shown in Figure 6B. The formal
537 error on the inversion σ^2 is extremely small, only 5×10^{-4}, although this value is a minimum and
538 does not include the 2% error from the FTIR area determination. The formal error σ^2 is not
539 always so small; see Table 1 for σ^2 as a function of grid spacing and λ for the San Carlos olivine
540 measurements discussed below and the Methods section for a description of simulations to assess
541 the true error in these simulations.

542 Results for the inverse model of the whole-block measurements produced a good fit to both
543 the whole-block and slice measurements with central values around the initial concentration, 34

This is a preprint, the final version is subject to change, of the American Mineralogist (MSA)
Cite as Authors (Year) Title. American Mineralogist, in press.
(DOI will not work until issue is live.) DOI: http://dx.doi.org/10.2138/am-2015-4847

544 ppm wt. H_2O, which is identical to the plateau in the SIMS measurements (Figure 5B). Thus,
545 there is strong coherence among the SIMS and FTIR measurements and the inverse approach for
546 solving for 3D concentration zonation within the whole block. These results agree with the
547 simulations showing that the central value of the 3D-WB measurements decreases from the
548 initial value of as a result of signal integration, while the true central value of the slice
549 measurements remains at the initial value.

550 The hydrogen diffusivities were then calculated by forward models from the whole-block
551 measurements (Table 2) using both 3D-WB and 3D-NPI approaches and from both the FTIR and
552 SIMS slice data using 1D models, which are adequate given that diffusion did not reach the
553 block center. The FTIR and SIMS slice data yield diffusivities that are within 0.1-0.2 log units of
554 each other. The 3D-WB analysis produced diffusivities that are within error but 0.1 to 0.5 orders
555 of magnitude slower than those determined from the slice measurements. In contrast to the
556 excellent agreement and fits of the whole-block and slice measurements analyses, 3D-NPI fits to
557 the whole-block measurements fail to accurately match the measurements, with a correlation
558 coefficient r^2 only 0.21 versus 0.64 for 3D-WB, and produce diffusivities almost an order of
559 magnitude too fast // [001] and about a factor of five too fast // [010]. Thus, given real
560 uncertainties in analytical measurements, the whole block effects can lead to order of magnitude
561 summed error in diffusivities when path integration effects are not taken into account.

562 Attempts to improve the fits by adjusting the diffusivities manually did not yield any clear
563 improvement because in 3D-WB analysis, the profiles are highly interdependent and often a
564 fundamentally different shape than in 3D-NPI. For instance, increasing $D_{[001]}$ to closely fit the
565 shape of the 3D-WB profile // [001] results in calculated profiles that are lower than most of the
566 central measurements // [010]. Also, the 3D-NPI fits cannot easily match the squat 3D-WB

This is a preprint, the final version is subject to change, of the American Mineralogist (MSA)
Cite as Authors (Year) Title. American Mineralogist, in press.
(DOI will not work until issue is live.) DOI: http://dx.doi.org/10.2138/am-2015-4847

profiles, and the resulting error is concentrated in the direction with the most well-developed profile, in agreement with the results of the numerical simulations.

An important source of uncertainty in these FTIR measurements arises from a change in the relative heights of the individual O-H stretching peaks, which are grouped together in this analysis to produce a single bulk hydrogen diffusivity. In some dehydration experiments, the final bulk absorbance area is as large or larger than the initial area measured at the same position and orientation. We attribute this change to a re-distribution of the hydrogen among different crystallographic environments similar to the changes first described in clinopyroxene by Skogby and Rossman (1989). A full peak analysis is beyond the scope of this paper, but this result emphasizes both the need for future work that considers O-H peaks individually and the potential importance of a pre-annealing (heating to dryness) and/or a hydrogen saturation step to allow the point defects to reach equilibrium prior to the main experiment.

Hydrogen diffusion in olivine

One potential application of the whole-block method is the diffusion of hydrogen in olivine, which is critical to how the mantle melts and deforms. Experimental measurements of hydrogen diffusion have been performed on San Carlos olivine (Mackwell and Kohlstedt 1990; Kohlstedt and Mackwell 1998; Demouchy and Mackwell 2006; Du Frane and Tyburczy 2012) and synthetic forsterite (Demouchy and Mackwell 2003; Padrón-Navarta et al. 2014). However, significant uncertainty remains about how best to interpret and apply these studies to obtain ascent rates based on olivine dehydration profiles (Le Voyer et al. 2014; Thoraval and Demouchy 2014). Here we apply the whole-block method to the hydration profiles of Demouchy

This is a preprint, the final version is subject to change, of the American Mineralogist (MSA)
Cite as Authors (Year) Title. American Mineralogist, in press.
(DOI will not work until issue is live.) DOI: http://dx.doi.org/10.2138/am-2015-4847

588 and Mackwell (2006) both to gain insight into the system and to provide an example of the
589 whole-block approach.

590 Although Demouchy and Mackwell (2006) interpreted their measurements using non-path-
591 integrated models, their concentration profiles were obtained through the whole block and must,
592 therefore, be revisited using models that take path integration effects into account. This task is
593 significantly complicated by the proposed existence of two separate hydrogen diffusion
594 mechanisms (Kohlstedt and Mackwell 1998): one ("proton-polaron") that is fast but short-lived
595 and dependent on ferric iron content and one ("proton-vacancy") that is relatively slow and
596 modeled as beginning once the fast mechanism saturates at a concentration value that Kohlstedt
597 and Mackwell (1998) call "metastable equilibrium". Isolating and quantifying diffusivities in this
598 sequential two mechanism model requires using the concentration of the final value in profiles
599 measured over short time scales as the initial profile for diffusion profiles measured over longer
600 times scales. Curiously, the slice profiles of Kohlstedt and Mackwell (1998) are not entirely
601 consistent with this approach (Figure 7), possibly as a result of changes in experimental oxygen
602 fugacity or differences in ferric iron content between their 1 hour and 8 hour samples. Demouchy
603 and Mackwell (2006) demonstrate the principle using a consistent set of experimental parameters
604 and 4 ppm wt. H_2O for "metastable equilibrium" (Figure 8A – DM06). However, 4 ppm is not a
605 reasonable initial value for fitting their 20 hour hydration profiles if the minimum concentration
606 in the sample is actually lower.

607 We applied the inverse tomographic method to these whole block measurements to solve for
608 the true central concentration using a $5 \times 9 \times 9$ grid, symmetry and smoothness model constraints
609 with a weighting parameter λ=0.05. Tomographic inverse modeling provides a good fit to these
610 measurements (Figure 6B) and indicates that the minimum value in this sample is 3.0 ± 0.1 ppm

This is a preprint, the final version is subject to change, of the American Mineralogist (MSA)
Cite as Authors (Year) Title. American Mineralogist, in press.
(DOI will not work until issue is live.) DOI: http://dx.doi.org/10.2138/am-2015-4847

611 wt. H_2O. This value is not in the exact center of the sample, consistent with higher measured
612 whole-block values in the center of the profile // [010] and perhaps indicating some
613 heterogeneity within the sample similar to that observed in the slice measurements of Kunlun
614 diopside. Note that the errors reported here include only the formal error on the inversion, σ_i, not
615 the calibration error on the original concentration estimates based on FTIR, which is on the order
616 of a few ppm wt. H_2O.

617 Approximately 25% of the observed 4 ppm wt. H_2O plateau value in the 20 hour San Carlos
618 olivine hydration profile of Demouchy and Mackwell (2006) is the result of signal integration
619 through the whole block. This difference, though trivial in absolute terms (3 ppm vs. 4 ppm wt.
620 H_2O, within calibration error for FTIR measurements), is important for two reasons. First, when
621 applying whole-block forward models and the sequential two mechanism model, 3 ppm wt. H_2O
622 is more appropriate than 4 ppm wt. H_2O as a transitional "metastable equilibrium" value. The
623 error in the central value translates directly into an error in the "metastable equilibrium" state,
624 and this error is preventable by applying the 3D-WB method. Second, there is actually an
625 inconsistency in the olivine measurements and their interpretation for a central value of 3 ppm
626 wt. H_2O. The metastable equilibrium model dictates that the olivine reaches a metastable
627 saturation value after 1 hour. This value is 3 and not 4 ppm H_2O, based on the inverse modeling
628 of the 3D-WB measurements. This interpretation is inconsistent with the maximum
629 concentrations in the 1 hour profiles (4 to 5 ppm wt. H_2O at the rims), which are certainly greater
630 than the central minimum concentration in the 20 hour sample (3 ppm wt. H_2O). This difference
631 cannot be dismissed as simply within error for FTIR because calibration error generally affects
632 all values the same way, i.e., all reported values are wrong by approximately the same amount in
633 only one direction. Thus, the model in which two diffusion mechanisms operate sequentially and

This is a preprint, the final version is subject to change, of the American Mineralogist (MSA)
Cite as Authors (Year) Title. American Mineralogist, in press.
(DOI will not work until issue is live.) DOI: http://dx.doi.org/10.2138/am-2015-4847

have some "metastable equilibrium" concentration is likely in error. At stake is not just an estimate of a particular diffusivity, but a fundamental understanding of how hydrogen diffuses in Fe-bearing olivine. Does diffusion proceed primarily by one dominant mechanism or multiple? Assuming multiple mechanisms are important, under what time scales do they operate, and to what extent can they be separated and individually quantified?

These questions are difficult to answer unambiguously with the available published profiles. Figure 8 shows a series of possible fits that all take path integration into account. In Figure 8A we show 3D-WB profiles that use the revised "metastable equilibrium" value of 3 ppm H_2O and the diffusivities from both the original interpretation of Demouchy and Mackwell (2006; labeled DM06 3D-WB) and Kohlstedt and Mackwell (1998; labeled KM98 3D-WB). The diffusivities from Demouchy and Mackwell (2006) provide a much better fit to this set of measurements (r^2=0.87) than the diffusivities of Kohlstedt and Mackwell (1998) (r^2=0.61). Two examples of possible alternative fits to the profiles from Demouchy and Mackwell (2006) are also shown in Figure 8: a single diffusion mechanism and two mechanisms that operate simultaneously and assume a fast mechanism that has diffusivities taken from Kohlstedt and Mackwell (1998) and saturates at 3 ppm wt. H_2O. These models provide slightly worse r^2 values than the 3D-WB revised sequential model (0.79 for single mechanism and 0.83 for simultaneous vs. 0.87), but they have the virtue of allowing the concentration at the rims in the 1 hour experiment (4-5 ppm wt. H_2O) to be greater than a "metastable equilibrium" value of 3 ppm H_2O. The single mechanism model is also much simpler to apply. Other fits are certainly possible, e.g., using different values at which the fast mechanism saturates or by varying the diffusivities, particularly for the rough 20 hour profiles // [100]. The original fits of Demouchy and Mackwell (2006) are very similar to many other models, including the one that applies the true central concentration

This is a preprint, the final version is subject to change, of the American Mineralogist (MSA)
Cite as Authors (Year) Title. American Mineralogist, in press.
(DOI will not work until issue is live.) DOI: http://dx.doi.org/10.2138/am-2015-4847

of 3 ppm H_2O as the "metastable equilibrium" starting concentration in the 20 hour experiments and the model using simultaneously operating mechanisms. This agreement arises because of the success of the 1D appoximation using the central 3D-WB plateau value (Figure 3), which is in essense what Demouchy and Mackwell (2006) did. Experiments that show greater diffusion progress would better enable distinction among the different models.

Two conclusions can be drawn from this exercise with regard to hydrogen diffusion in olivine. First, taken in isolation, the hydration profiles reported by Demouchy and Mackwell (2006) can be adequately modeled by a relatively simple (and therefore preferable) single mechanism model. Second, none of the modeling approaches discussed here can satisfactorily explain or reconcile the large (0.9 to 1.8 orders of magnitude) discrepancy between the slow mechanism hydrogen diffusivity in San Carlos olivine observed by Demouchy and Mackwell (2006) and that observed by Kohlstedt and Mackwell (1998) and in forsterite (Figure 10 and Table 3). In particular, Kohlstedt and Mackwell (1998) show a clear change in anisotropy in San Carlos olivine from a fast direction // [100] at 1 hour to a fast direction // [001] at 8 hours that is not as readily apparent in the Demouchy and Mackwell (2006) profiles. Additional experiments, especially those that consider site-specific diffusivity as in Padrón-Navarta et al. (2014), are required to fully understand this system.

Implications

A new treatment of whole-block measurements successfully yields hydrogen diffusivities in three orthogonal directions of a rectangular prism without cutting the sample. This approach will simplify future diffusion experiments that rely on FTIR and be bolstered by the results of measurements from cut samples. Multiple hydrogen diffusion experiments are now possible

679 using the same sample (e.g., a time series using profiles), which will minimize both the amount
680 of sample material needed and the error associated with heterogeneity among samples from the
681 same locale. The efficacy of the method has been demonstrated experimentally for hydrogen
682 diffusion in diopside. Because the differences between whole-block and slice measurements are
683 often significant, path integration effects must be considered when evaluating whole-block
684 measurements. Failure to include these path integration effects may result in errors of half an
685 order of magnitude or more in fast and/or short directions. In cases where diffusion has not
686 progressed significantly, it is possible to use a 1D approximation with the whole-block central
687 plateau to accurately obtain diffusivities with errors less than 0.5 log units because diffusivities
688 are more sensitive to profile shape than the absolute concentration of the central plateau.
689 However, in cases where absolute concentrations are required, forward or inverse 3D-WB
690 models are necessary to recover core concentrations. An important application of these effects is
691 in the interpretation of olivine diffusion experiments. We use the new whole block forward and
692 inverse methods to re-evaluate whole block measurements of olivine dehydration (Demouchy
693 and Mackwell 2006). The resulting diffusivities are within the range of those originally
694 published for the slower "proton-vacancy" mechanism, but could also be consistent with a
695 simpler single diffusive mechanism. The newly determined central value concentrations create
696 inconsistencies with existing interpretations of dual mechanisms and "metastable equilibrium"
697 concentrations. The whole-block approach is likely to prove very useful for future work on
698 olivine, pyroxene, and other nominally anhydrous minerals to illuminate the parameters that
699 define different hydrogen diffusion mechanisms (particularly the role of differing
700 crystallographic environments as in Padrón-Navarta et al. 2014) for use in broader Earth science
701 applications such as determining crystal residence times (Danyushevsky et al. 2002), magma

degassing rates (Hauri 2002), and ascent times (Demouchy et al. 2006, Peslier and Luhr 2006, Denis et al. 2013, Chen et al. 2013); interpreting hydrogen concentrations in melt inclusions (Portnyagin et al. 2008, Chen et al. 2011, Gaetani et al. 2012, Bucholz et al. 2013, Lloyd et al. 2013) and mantle xenoliths (review by Peslier 2010); and electrical conductivity (e.g., Karato 1990).

Acknowledgements

This work was supported by National Science Foundation postdoctoral research fellowship award number 1049587 to Ferriss. We thank George Harlow for providing the diopside sample (American Museum of Natural History sample #100242), Beth Goldoff for providing assistance with the FTIR, Alex Lloyd and Erik Hauri for providing the SIMS analyses, and Denton Ebel for the use of his tungsten-wire saw. This manuscript benefited from detailed reviews by Sylvie Demouchy, an anonymous reviewer, and managing editor Fidel Costa.

References cited

Anovitz, L.M., Elam, J.M., Riciputi, L.R., and Cole, D.R. (1999) The failure of obsidian hydration dating: Sources, implications, and new directions. Journal of Archaeological Science, 26, 735-752.

Ardia, P., Hirschmann, M., Withers, A.C., and Tenner, T.J. (2012) H_2O storage capacity of olivine at 5-8GPa and consequences for dehydration partial melting of the upper mantle. Earth and Planetary Science Letters, 345-348, 104-116.

721 Aubaud, C., Withers, A.C., Hirschmann, M.M., Guan, Y.B., Leshin, L.A., Mackwell, S.J., and
722 Bell, D.R. (2007) Intercalibration of FTIR and SIMS for hydrogen measurements in
723 glasses and nominally anhydrous minerals. American Mineralogist, 92, 811-828.
724 Bell, D.R., Ihinger, P.D., and Rossman, G.R. (1995) Quantitative analysis of trace OH in garnet
725 and pyroxenes. American Mineralogist, 80, 465-474.
726 Bell, D.R., Rossman, G.R., Maldener, J., Endisch, D., and Rauch, F. (2003) Hydroxide in
727 olivine: A quantitative determination of the absolute amount and calibration of the IR
728 spectrum. Journal of Geophysical Research-Solid Earth, 108, B2.
729 Berry, A.J., Walker, A.M., Hermann, J., O'Neill, H.S., Foran, G.J., and Gale, J.D. (2007)
730 Titanium substitution mechanisms in forsterite. Chemical Geology, 242, 176-186.
731 Bucholz, C.E., Gaetani, G.A., Behn, M.D., and Shimizu, N. (2013) Post-entrapment modification
732 of volatiles and oxygen fugacity in olivine-hosted melt inclusions. Earth and Planetary
733 Science Letters, 374, 145-155.
734 Carslaw, H.S. and Jaeger, J.C. (1959) Conduction of heat in solids. Oxford, U.K., Clarendon.
735 Chen, Y., Provost, A., Schiano, P., and Cluzel, N. (2011) The rate of water loss from olivine-
736 hosted melt inclusions. Contributions to Mineralogy and Petrology, 162, 625-636.
737 Chen, Y., Provost, A., Schiano, P., and Cluzel, N. (2013) Magma ascent rate and initial water
738 concentration inferred from diffusive water loss from olivine-hosted melt inclusions.
739 Contributions to Mineralogy and Petrology, 165, 525-541.
740 Crank, J. (1975) The mathematics of diffusion. Oxford, Oxford University Press.
741 Danyushevsky, L.V., McNeill, A.W., and Sobolev, A.V. (2002) Experimental and petrological
742 studies of metld inclusions in phenocrysts from mantle-derived magmas: An overview of
743 techniques, advantages and complications. Chemical Geology, 183, 5-24.

744 Deines, P., Nafziger, R.H., Ulmer, G.C., and Woermann, E. (1974). Temperature - oxygen
745 fugacity tables for selected gas mixtures in the system C-H-O at on atmosphere total
746 pressure. Bulletin of the earth and mineral sciences experiment station. University Park,
747 Pennsylvania, The Pennsylvania State University. 88.
748 Demouchy, S., Jacobsen, S.D., Gaillard, F., and Stern, C.R. (2006) Rapid magma ascent
749 recorded by water diffusion profiles in mantle olivine. Geology, 34, 429-432.
750 Demouchy, S. and Mackwell, S. (2003) Water diffusion in synthetic iron-free forsterite. Physics
751 and Chemistry of Minerals, 30, 486-494.
752 Demouchy, S. and Mackwell, S. (2006) Mechanisms of hydrogen incorporation and diffusion in
753 iron-bearing olivine. Physics and Chemistry of Minerals, 33, 347-355.
754 Denis, C.M.M., Demouchy, S., and Shaw, C.S.J. (2013) Evidence of dehydration in peridotites
755 from Eifel Volcanic Field and estimates of the rate of magma ascent. Journal of
756 Volcanology and Geothermal Research, 258, 85-99.
757 Doremus, R.H. (1975) Interdiffusion of hydrogen and alkali ions in a glass surface. Journal of
758 Non-Crystalline Solids, 19, 137-144.
759 Dyar, M.D., McGuire, A.V., and Ziegler, R.D. (1989) Redox equilibria and crystal-chemistry of
760 coexisting minerals from spinel lherzolite mantle xenoliths. American Mineralogist, 74,
761 969-980.
762 Farver, J.R. (2010). Oxygen and Hydrogen Diffusion in Minerals. Diffusion in Minerals and
763 Melts. Y. X. Zhang and D. J. Cherniak. Chantilly, Mineralogical Soc Amer. 72: 447-507.
764 Ferot, A. and Bolfan-Casanova, N. (2012) Water storage capacity in olivine and pyroxene to 14
765 GPa: Implications for the water content of the Earth's upper mantle and nature of seismic
766 discontinuities. Earth and Planetary Science Letters, 349, 218-230.

767 Gaetani, G.A., O'Leary, J.A., Shimizu, N., Bucholz, C.E., and Newville, M. (2012) Rapid
768 reequilibration of H_2O and oxygen fugacity in olivine-hosted melt inclusions. Geology,
769 40, 915-918.
770 Grzechnik, A., Zimmermann, H.D., Hervig, R.L., King, P.L., and McMillan, P.F. (1996) FTIR
771 micro-reflectance measurements of the CO_3^{2-} ion content in basanite and leucitite glasses.
772 Contributions to Mineralogy and Petrology, 125, 311-318.
773 Hauri, E. (2002) SIMS analysis of volatiles in silicate glasses, 2: isotopes and abundances in
774 Hawaiian melt inclusions. Chemical Geology, 183, 115-141.
775 Hervig, R., Mazdab, F.K., Moore, R.O., and McMillan, P.F. (2003). Analyzing hydrogen (H_2O)
776 in silicate glass by secondary ion mass spectrometry and reflectance Fourier transform
777 infrared spectroscopy. Melt Inclusions in Volcanic Systems: Methods, Applications, and
778 Problems. B. de Vivo and R. J. Bodnar. Amsterdam, Elsevier: 83-103.
779 Hofmann, A.E. (1980). Diffusion in silicate melts: A critical review. Physics of magmatic
780 processes. R. B. Hargraves. Princeton, NJ, Princeton University Press: 385-418.
781 Ingrin, J. and Blanchard, M. (2006). Diffusion of hydrogen in minerals. Water in Nominally
782 Anhydrous Minerals. H. Keppler and J. R. Smyth, Mineralogical Society of America. 62:
783 291-320.
784 Ingrin, J., Hercule, S., and Charton, T. (1995) Diffusion of hydrogen in diopside - Results of
785 dehydration experiments. Journal of Geophysical Research-Solid Earth, 100, 15489-
786 15499.
787 King, P.L. and Larsen, J. (2013) A micro-reflectance IR spectroscopy method for analyzing
788 volatile species in basaltic, andesitic, phonolitic, and rhyolitic glasses. American
789 Mineralogist, 98, 1162-1171.

790 Kohlstedt, D., Keppler, H., and Rubie, D.C. (1996) Solubility of water in the alpha, beta, and
791 gamma phases of $(Mg,Fe)_2SiO_4$. Contributions to Mineralogy and Petrology, 123, 345-
792 357.
793 Kohlstedt, D.L. and Mackwell, S.J. (1998) Diffusion of hydrogen and intrinsic point defects in
794 olivine. Zeitschrift Fur Physikalische Chemie-International Journal of Research in
795 Physical Chemistry & Chemical Physics, 207, 147-162.
796 Kovacs, I., Hermann, J., O'Neill, H.S.C., Fitz Gerald, J.D., Sambridge, M., and Horvath, G.
797 (2008) Quantitative absorbance spectroscopy with unpolarized light: Part II.
798 Experimental evaluation and development of a protocol for quantitative analysis of
799 mineral IR spectra. American Mineralogist, 93, 765-778.
800 Kovacs, I., O'Neill, H.S.C., Hermann, J., and Hauri, E.H. (2010) Site-specific infrared O-H
801 absorption coefficients for water substitution into olivine. American Mineralogist, 95,
802 292-299.
803 Lanford, W.A., Davis, K., Lamarche, P., Laursen, T., Groleau, R., and Doremus, R.H. (1979)
804 Hydration of sode lime glass. Journal of Non-Crystalline Solids, 33, 249-266.
805 Libowitzky, E. and Rossman, G.R. (1996) Principles of quantitative absorbance measurements in
806 anisotropic crystals. Physics and Chemistry of Minerals, 23, 319-327.
807 Libowitzky, E. and Rossman, G.R. (1997) An IR absorption calibration for water in minerals.
808 American Mineralogist, 82, 1111-1115.
809 Lloyd, A.S., Plank, T., Ruprecht, P., Hauri, E.H., and Rose, W. (2013) Volatile loss from melt
810 inclusions in pyroclasts of differing sizes. Contributions to Mineralogy and Petrology,
811 165, 129-153.

812 Lowenstern, J.B. and Pitcher, B.W. (2013) Analysis of H_2O in silicate glass using attenuated
813 total reflectance (ATR) micro-FTIR spectrascopy. American Mineralogist, 98, 1660-
814 1668.
815 Mackwell, S.J. and Kohlstedt, D.L. (1990) Diffusion of hydrogen in olivine - implications for
816 water in the mantle. Journal of Geophysical Research-Solid Earth and Planets, 95, 5079-
817 5088.
818 Mei, S. and Kohlstedt, D.L. (2000) Influence of water on plastic deformation of olivine
819 aggregates 1. Diffusion creep regime. Journal of Geophysical Research-Solid Earth, 105,
820 21457-21469.
821 Mei, S. and Kohlstedt, D.L. (2000) Influence of water on plastic deformation of olivine
822 aggregates 2. Dislocation creep regime. Journal of Geophysical Research-Solid Earth,
823 105, 21471-21481.
824 Miller, G.H., Rossman, G.R., and Harlow, G.E. (1987) The natural occurrance of hydroxide in
825 olivine. Physics and Chemistry of Minerals, 14, 461-472.
826 Mosenfelder, J.L., Deligne, N.I., Asimow, P.D., and Rossman, G.R. (2006) Hydrogen
827 incorporation in olivine from 2-12 GPa. American Mineralogist, 91, 285-294.
828 Padrón-Navarta, J.A., Hermann, J., and O'Neill, H.S.C. (2014) Site-specific hydrogen diffusion
829 rates in forsterite. Earth and Planetary Science Letters, 392, 100-112.
830 Paterson, M.S. (1982) The determination of hydroxyl by infrared absorption in quartz, slicate
831 glasses and similar materials. Bulletin De Mineralogie, 105, 20-29.
832 Peslier, A.H. and Luhr, J.F. (2006) Hydrogen loss from olivines in mantle xenoliths from Simcoe
833 (USA) and Mexico: Mafic alkalic magma ascent rates and water budget of the sub-
834 continental lithosphere. Earth and Planetary Science Letters, 242, 302-319.

835 Peslier, A.H. (2010) A review of water contents of nominally anhydrous natural minerals in the
836 mantles of Earth, Mars and the Moon. Journal of Volcanology and Geothermal Research,
837 197, 239-258.
838 Portnyagin, M., Almeev, R., Matveev, S., and Holtz, F. (2008) Experimental evidence for rapid
839 water exchange between melt inclusions in olivine and host magma. Earth and Planetary
840 Science Letters, 272, 541-552.
841 Rossman, G.R. (2006). Analytical methods for measuring water in nominally anhydrous
842 minerals. Water in Nominally Anhydrous Minerals. H. Keppler and J. R. Smyth.
843 Chantilly, Mineralogical Society of America, 62: 1-28.
844 Ryerson, F.J. (1987). Diffusion measurements: Experimental Methods. Methods of Experimental
845 Physics, Academic Press, Inc. 24, Part A: 89-130.
846 Sambridge, M., Gerald, J.F., Kovacs, I., O'Neill, H.S.C., and Hermann, J. (2008) Quantitative
847 absorbance spectroscopy with unpolarized light: Part I. Physical and mathematical
848 development. American Mineralogist, 93, 751-764.
849 Skogby, H. and Rossman, G.R. (1989) OH- in pyroxene - An experimental study of
850 incorporation mechanisms and stability. American Mineralogist, 74, 1059-1069.
851 Van Orman, J.A., Grove, T.L., and Shimizu, N. (1998) Uranium and thorium diffusion in
852 diopside. Earth and Planetary Science Letters, 160, 505-519.
853 Van Orman, J.A., Grove, T.L., and Shimizu, N. (2001) Rare earth element diffusion in diopside:
854 influence of temperature, pressure, and ionic radius, and an elastic model for diffusion in
855 silicates. Contributions to Mineralogy and Petrology, 141, 687-703.

856 Wade, J.A., Plank, T., Hauri, E.H., Kelley, K.A., Roggensack, K., and Zimmer, M. (2008)
857 Prediction of magmatic water contents via measurement of H_2O in clinopyroxene
858 phenocrysts. Geology, 36, 799-802.
859 Walker, A.M., Hermann, J., Berry, A.J., and O'Neill, H.S. (2007) Three water sites in upper
860 mantle olivine and the role of titanium in the water weakening mechanism. Journal of
861 Geophysical Research-Solid Earth, 112,
862 Wang, L.P., Zhang, Y.X., and Essene, E.J. (1996) Diffusion of the hydrous component in
863 pyrope. American Mineralogist, 81, 706-718.
864 Watson, E.B. and Baxter, E.F. (2007) Diffusion in solid-earth systems. Earth and Planetary
865 Science Letters, 253, 307-327.
866 Watson, E.B. and Dohmen, R. (2010). Non-traditional and emerging methods for characterizing
867 diffusion in minerals and mineral aggregates. Diffusion in Minerals and Melts. Y. X.
868 Zhang and D. J. Cherniak. Chantilly, Mineralogical Society of America, 72: 61-106.
869 Withers, A.C. (2013) On the use of unpolarized infrared spectroscopy for quantitative analysis of
870 absorbing species in birefringent crystals. American Mineralogist, 98, 689-697.
871 Withers, A.C., Hirschmann, M.M., and Tenner, T.J. (2011) The effect of Fe on olivine H_2O
872 storage capacity: Consequences for H_2O in the martian mantle. American Mineralogist,
873 96, 1039-1053.
874 Woods, S.C., Mackwell, S., and Dyar, D. (2000) Hydrogen in diopside: Diffusion profiles.
875 American Mineralogist, 85, 480-487.
876 Xia, Q.K., Liu, J., Liu, S.C., Kovacs, I., Feng, M., and Dang, L. (2013) High water content in
877 Mesozoic primitive basalts of the North China Craton and implications on the destruction
878 of cratonic mantle lithosphere. Earth and Planetary Science Letters, 361, 85-97.

879 Zhang, Y. and Cherniak, D.J., Eds. (2010). Diffusion in minerals and melts. Reviews in
880 mineralogy and geochemistry, Mineralogical Society of America, Geochemical Society.
881 Zhang, Y.X., Stolper, E.M., and Wasserburg, G.J. (1991) Diffusion of water in rhyolitic glasses.
882 Geochimica Et Cosmochimica Acta, 55, 441-456.
883 Zhao, Y.H., Ginsberg, S.B., and Kohstedt, D.L. (2004) Solubility of hydrogen in olivine:
884 dependence on temperature and iron content. Contributions to Mineralogy and Petrology,
885 147, 155-161.
886

This is a preprint, the final version is subject to change, of the American Mineralogist (MSA)
Cite as Authors (Year) Title. American Mineralogist, in press.
(DOI will not work until issue is live.) DOI: http://dx.doi.org/10.2138/am-2015-4847

887 **List of figure captions**

888 Figure 1. Sketch showing representative depth slices of an initially dry rectangular prism
889 that has been partially hydrated during a diffusion experiment. The whole-block approach
890 developed here evaluates measurements derived from signals that are transmitted and absorbed
891 by all the layers of the entire sample along the transmission direction rather than cutting a slice
892 from the center of the sample.
893
894 Figure 2. Sensitivity maps showing summed error in the diffusivities on a log scale for fits to
895 simulated 3D-WB data using a diffusion model that does not take path integration into account
896 (the 3D-NPI model) (A) for isotropic diffusion as a function of sample shape and diffusion
897 progress and (B) in an equant crystal as a function of anisotropy and diffusion progress. Example
898 profiles are labeled and shown below each map. In all simulations, the diffusing species is
899 entering the sample, the initial concentration is 0, and the equilibrium concentration is S. D
900 values are the initial diffusivities in m^2/s used to simulate the 3D-WB data (only 20 simulated
901 data points out of 100 are shown for clarity) in each orthogonal direction ([100], [010], and
902 [001]; length of crystal along [100] is 2.2 mm in all examples), and D_{fit} is the diffusivity in each
903 direction in m^2/s determined using a least-squares best-fit to the 3D-NPI model. Ray paths R are
904 // [010] for profiles // [100], R // [100] for profiles // [010], and R // [100] for profiles // [001].
905 For comparison, simulated slice profiles (from 3D-NPI equations) are shown for each example.
906
907 Figure 3. Sensitivity maps calculated using the same numerical simulation approach as in
908 Figure 2 showing summed error in the diffusivities for a set of three 1D-NPI models fit to 3D-

This is a preprint, the final version is subject to change, of the American Mineralogist (MSA)
Cite as Authors (Year) Title. American Mineralogist, in press.
(DOI will not work until issue is live.) DOI: http://dx.doi.org/10.2138/am-2015-4847 10/7

WB data using the the 3D-WB plateau concentration in place of the true initial value (zero), thus ignoring the apparent drop in the 3D-WB central concentration and emphasizing the profile curvature, which is what primarily determines the calculated diffusivities.

Figure 4. Simulated diffusion profiles for the hydration of an initially dry cube in which diffusion is strongly anisotropic. *D* is diffusivity in each direction, and *R* is the direction of the ray path of the infrared beam. See Movies 2 and 3 for changes in diffusion profiles with time.

Figure 5. Concentration profiles in diopside after partial dehydration for 75 hours at 1000 °C measured using unpolarized FTIR and SIMS for (A) the uncut block (3D-WB) and (B) a slice cut from the center of the sample. Diffusivities (D) were determined by least square fits in each direction for the 3D-WB FTIR measurements using both the 3D-WB model and the non-path-integrated 3-dimensional model (3D-NPI) and for the slice FTIR and SIMS measurements using 3D-NPI models. The initial concentration is assumed to be 34 ppm wt. H_2O and uniform, and the equilibrium concentration is assumed to be 0. The measurements are provided in Supplementary Table 1, and error estimates and correlation coefficients are listed in Table 2.

Figure 6. (A) Results of inverse analyses showing FTIR 3D-WB measurements, predicted values based on inverse model results, and associated residuals for the dehydrated Kunlun diopside from this study. (B) FTIR measurements of a slice cut from the center of the sample and predicted values based on inverse analysis. Light grey dashed lines show the sub-divisions in the $9 \times 9 \times 9$ grid used to model the system, where each block is assumed to contain a uniform concentration. Propagated errors plot within the symbols.

This is a preprint, the final version is subject to change, of the American Mineralogist (MSA)
Cite as Authors (Year) Title. American Mineralogist, in press.
(DOI will not work until issue is live.) DOI: http://dx.doi.org/10.2138/am-2015-4847

932

933 Figure 7. Hydrogen profiles // [100] from central slice FTIR measurements reproduced from
934 Kohlstedt and Mackwell (1998). The original paper used a value of 7 H/10^6Si (red line) as the
935 initial value when fitting the 8 hour data, but this "metastable equilibrium" value cannot also be
936 used as the final value to fit their 1 hour data. Note the different temperatures, pressures, and
937 oxygen fugacities of the two experiments.

938

939 Figure 8. Whole-block FTIR measurements (squares) for hydrogen diffusion experiments at
940 1 and 20 hours on San Carlos olivine at 200 MPa, the Ni/NiO buffer, 900 °C, and observed
941 initial concentration C_i=0 reproduced from Demouchy and Mackwell (2006), and five different
942 approaches to modeling diffusivities based on these profiles. Error bars are shown in the original
943 text and are omitted here for clarity. (A) "DM06" is the original fit by Demouchy and Mackwell
944 (2006) that does not consider path integration effects and uses 4 ppm wt. H_2O (dotted grid line)
945 as a transitional state between two mechanisms. "DM06 3D-WB" uses the diffusivities estimated
946 from the original fit with the whole-block forward model and a transitional state of 3 ppm wt.
947 H_2O (the central value in the sample determined by tomography; see text). "KM98 3D-WB" uses
948 an identical approach as "DM06 3D-WB" except the diffusivities are those expected from
949 Kohlstedt and Mackwell (1998). "Single mech." illustrates a possible fit to both the 1 hour and
950 20 hour profiles using the same diffusivity, initial concentration, and solubility for both sets of
951 concentration profiles. (B) Shows the two mechanisms described by Demouchy and Mackwell
952 (2006) modeled as operating simultaneously rather than sequentially. For simplicity and
953 consistency with previous work, the fast mechanism diffusivities (mech. 1) were held constant at
954 the values expected based on Kohlstedt and Mackwell (1998), and best fit slow diffusivities were

This is a preprint, the final version is subject to change, of the American Mineralogist (MSA)
Cite as Authors (Year) Title. American Mineralogist, in press.
(DOI will not work until issue is live.) DOI: http://dx.doi.org/10.2138/am-2015-4847

obtained by fitting to both sets of profiles simultaneously. The diffusivity estimates for all models are given in Table 3 and plotted on an Arrhenius diagram in Figure 10.

Figure 9. Observed whole-block measurements for hydrogen diffusion in San Carlos olivine (Demouchy and Mackwell 2006) after 20 hours at 900 °C, predicted whole-block measurements based on inverse model results, and associated residuals. Light grey dashed lines show the sub-divisions in the 5 × 9 × 9 grid used to model the profiles, where each block is assumed to contain a uniform concentration. Propagated errors on the predicted values plot within the symbols.

Figure 10. Arrhenius diagram of hydrogen diffusivity measurements in olivine. Self-diffusivity is from Du Frane and Tyburczy (2012). New diffusivity estimates from this study (Figure 8) based on the measurements of Demouchy and Mackwell (2006; labeled DM06) are shown for both the assumption of a single diffusion mechanism and for a slow mechanism assumed to operate simultaneously with the fast mechanism of Kohlstedt and Mackwell (1998; labeled KM98). PN is Padrón-Navarta et al. (2014), and bracketed elements in PN refer to different H defects inferred from FTIR absorption bands. The five studies in which orientation was not determined (Padrón-Navarta et al. 2014, Gaetani et al. 2012, Hauri 2002, Chen et al. 2011, and Portnyagin et al. 2008, who report a minimum diffusivity) are plotted only on the first panel for comparison.

List of table headings

Table 1. The number of grid cells parallel to each direction and constraint weighting factor λ used to model the 20 hour San Carlos olivine hydrogen profiles from Demoucy and Mackwell

This is a preprint, the final version is subject to change, of the American Mineralogist (MSA)
Cite as Authors (Year) Title. American Mineralogist, in press.
(DOI will not work until issue is live.) DOI: http://dx.doi.org/10.2138/am-2015-4847

977 (2006), resulting goodness of fit parameter σ^2, and estimated minimum concentration in the
978 center in ppm wt. H_2O.
979
980 Table 2. Diffusivities (D in m^2/s), associated errors, and correlation coefficients (r^2)
981 determined for Kunlun diopside at 1000°C using four different approaches. "3D-WB" is the
982 whole-block path-integrated forward model. "1D" and "3D-NPI" are 1- and 3-dimensional non-
983 path-integrated models. The reported errors are based on 95% confidence intervals in the fitting
984 procedure. Diffusivity estimates // [100]* from slice measurements are not available and are
985 labeled "N/A".
986
987 Table 3. Diffusivity estimates in m^2/s for various forward models (Figure 8) to the whole-
988 block measurements of Demouchy and Mackwell (2006). Diffusivities reported by Kohlstedt and
989 Mackwell (1998) are provided for comparison.
990
991 Supplementary Table 1. Hydrogen concentration as a function of position in heat-treated
992 Kunlun diopside. Total lengths are 3450±10 μm // [100]*, 1609±5 μm // [010], and 1757±6 μm //
993 [001]. FTIR measurements are reported assuming a uniform initial concentration of 34 ppm wt.
994 H_2O. Slice data were not available // [100]* and are labeled "N/A".
995

Fig 1

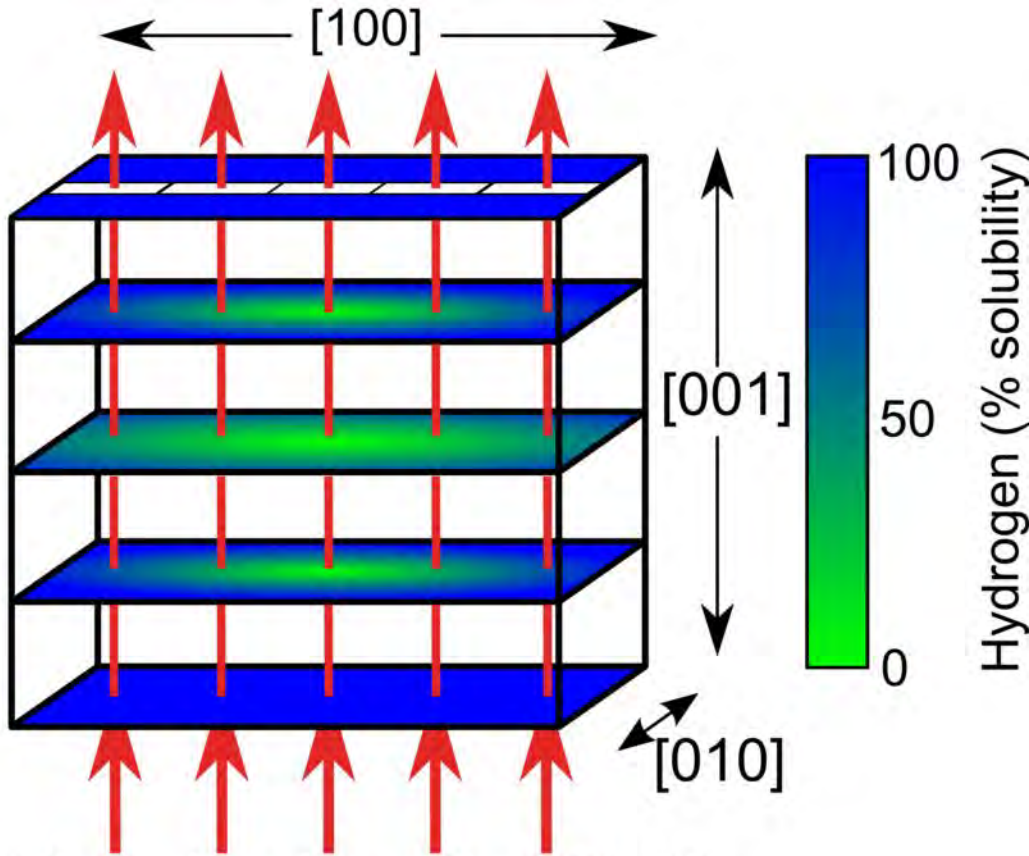

Whole-block profile // [100]
with ray path R // [001]

fig 2

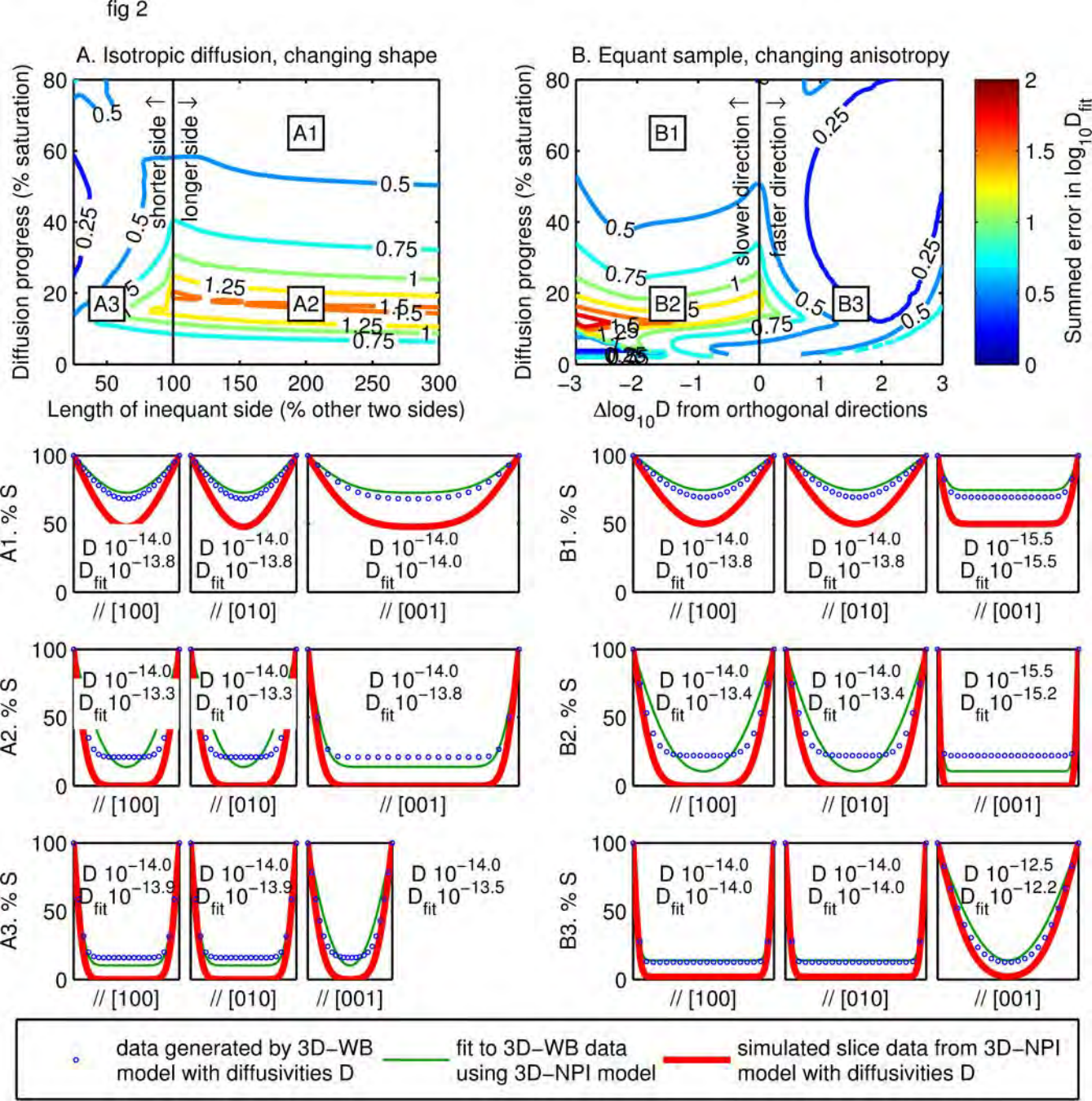
A. Isotropic diffusion, changing shape
B. Equant sample, changing anisotropy
Diffusion progress (% saturation)
Length of inequant side (% other two sides)
shorter side →
longer side →
A1
A2
A3
B1
B2
B3
slower direction →
faster direction →
Δlog10D from orthogonal directions
Summed error in log10Dfit
A1. % S
A2. % S
A3. % S
B1. % S
B2. % S
B3. % S
// [100]
// [010]
// [001]
data generated by 3D−WB model with diffusivities D
fit to 3D−WB data using 3D−NPI model
simulated slice data from 3D−NPI model with diffusivities D

Fig 3 (1D plateau approximation)

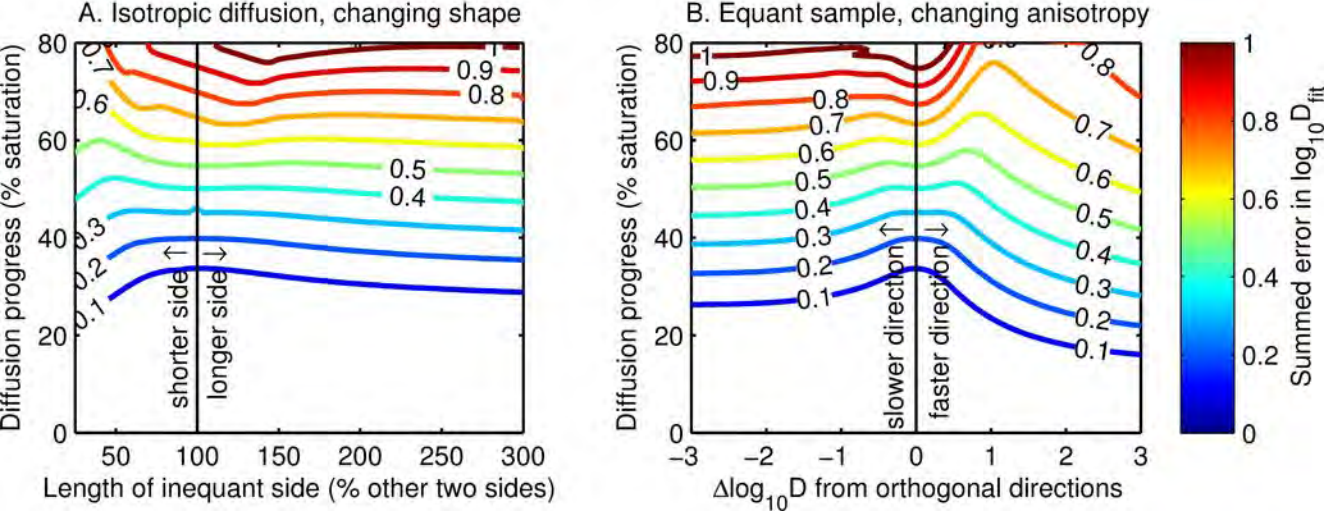

fig 4

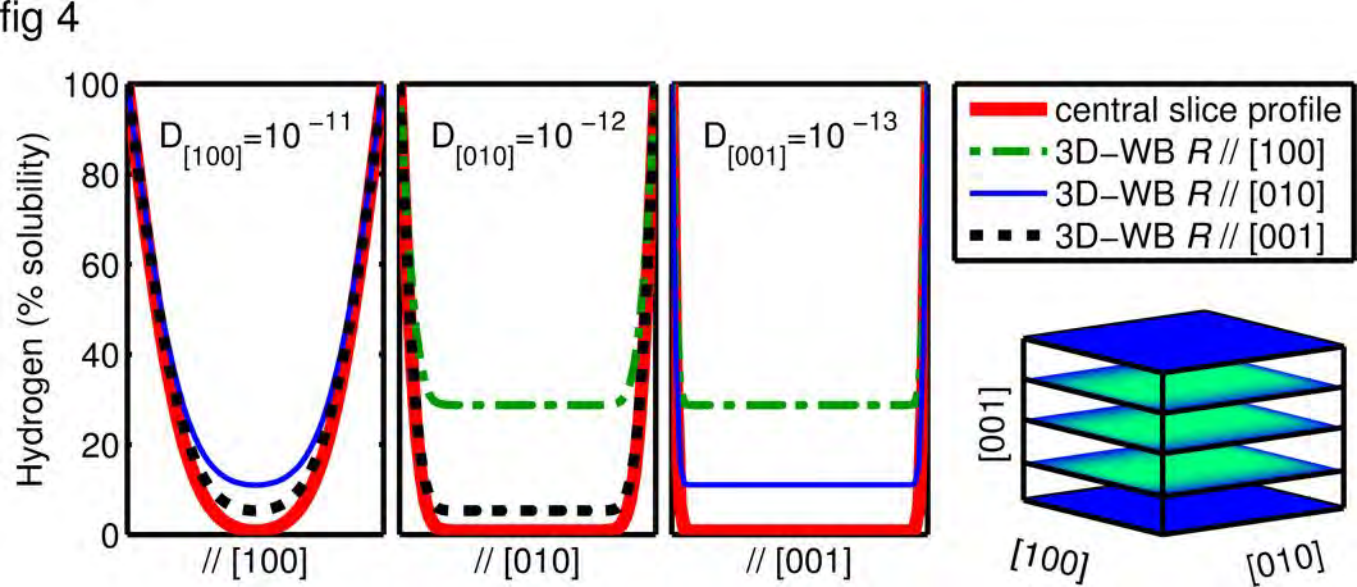
Hydrogen (% solubility)
100
80
60
40
20
0
D[100]=10 −11
D[010]=10 −12
D[001]=10 −13
// [100]
// [010]
// [001]
central slice profile
3D–WB R // [100]
3D–WB R // [010]
3D–WB R // [001]
[001]
[100]
[010]

Fig 5

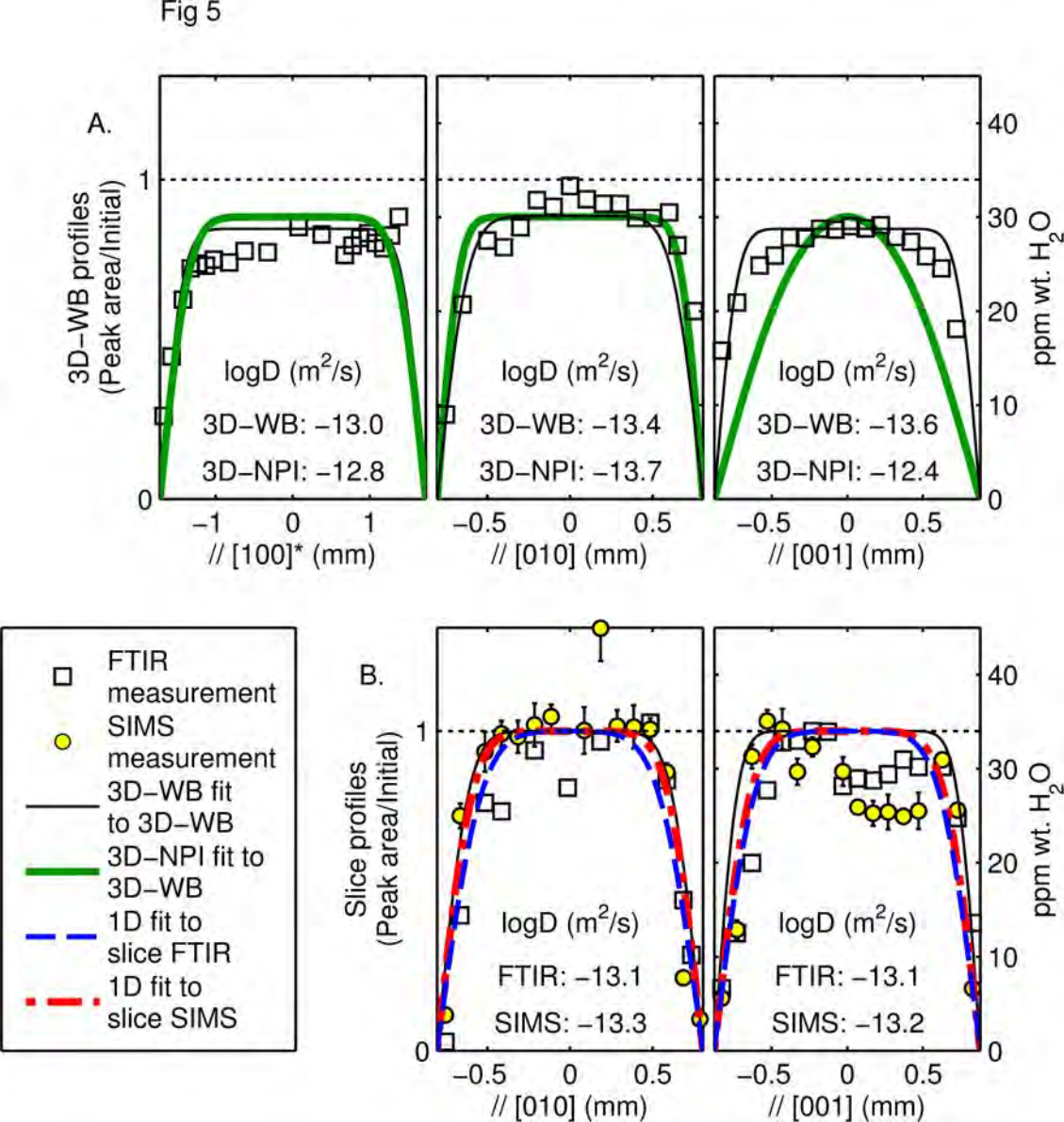
A.
3D–WB profiles (Peak area/Initial)
ppm wt. H_2O
logD (m^2/s)
3D–WB: –13.0
3D–NPI: –12.8
// [100]* (mm)
logD (m^2/s)
3D–WB: –13.4
3D–NPI: –13.7
// [010] (mm)
logD (m^2/s)
3D–WB: –13.6
3D–NPI: –12.4
// [001] (mm)
FTIR measurement
SIMS measurement
3D–WB fit to 3D–WB
3D–NPI fit to 3D–WB
1D fit to slice FTIR
1D fit to slice SIMS
B.
Slice profiles (Peak area/Initial)
ppm wt. H_2O
logD (m^2/s)
FTIR: –13.1
SIMS: –13.3
// [010] (mm)
logD (m^2/s)
FTIR: –13.1
SIMS: –13.2
// [001] (mm)

Fig 6

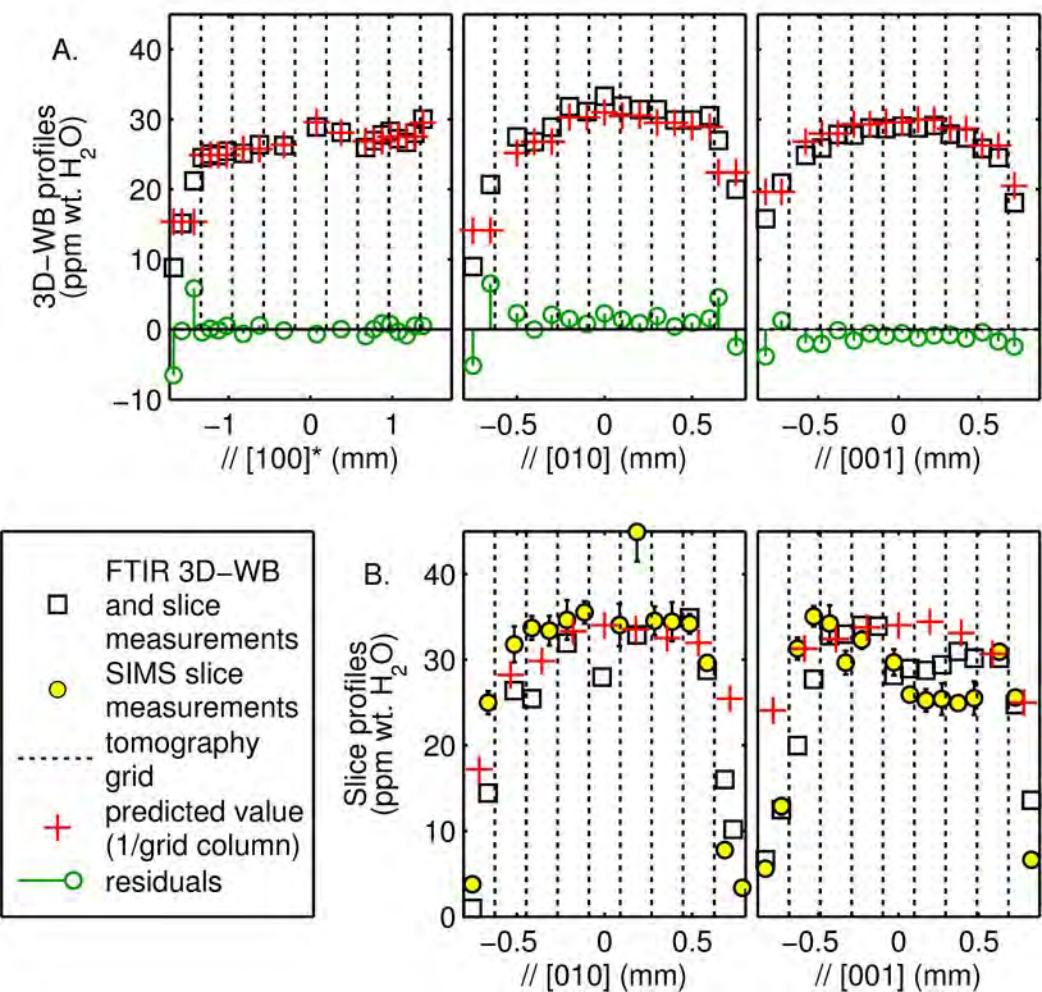
A.
3D−WB profiles (ppm wt. H_2O)
40
30
20
10
0
−10
−1
0
1
// [100]* (mm)
−0.5
0
0.5
// [010] (mm)
−0.5
0
0.5
// [001] (mm)
FTIR 3D−WB and slice measurements
SIMS slice measurements
tomography grid
predicted value (1/grid column)
residuals
B.
Slice profiles (ppm wt. H_2O)
40
30
20
10
0
−0.5
0
0.5
// [010] (mm)
−0.5
0
0.5
// [001] (mm)

Fig 7

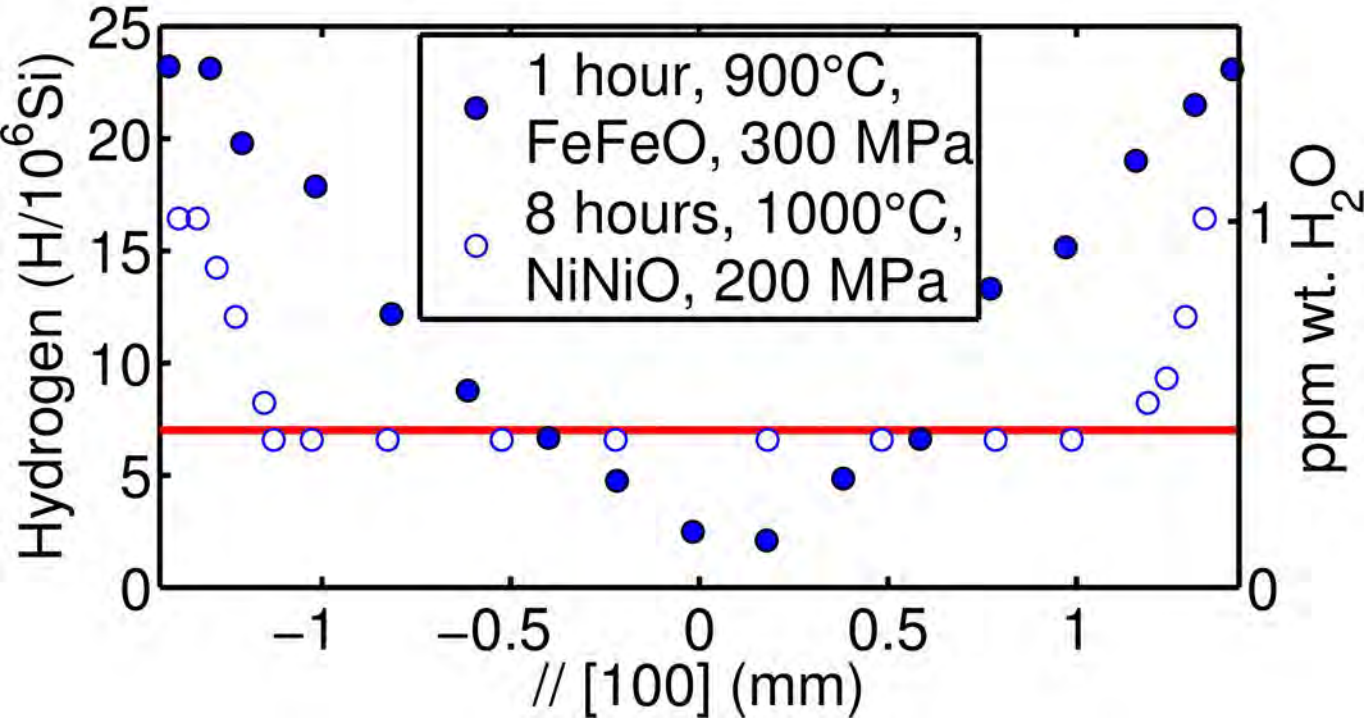
1 hour, 900°C,
FeFeO, 300 MPa
8 hours, 1000°C,
NiNiO, 200 MPa
Hydrogen (H/10^6Si)
ppm wt. H2O
// [100] (mm)
25
20
15
10
5
0
1
0
−1
−0.5
0
0.5
1

Fig 8

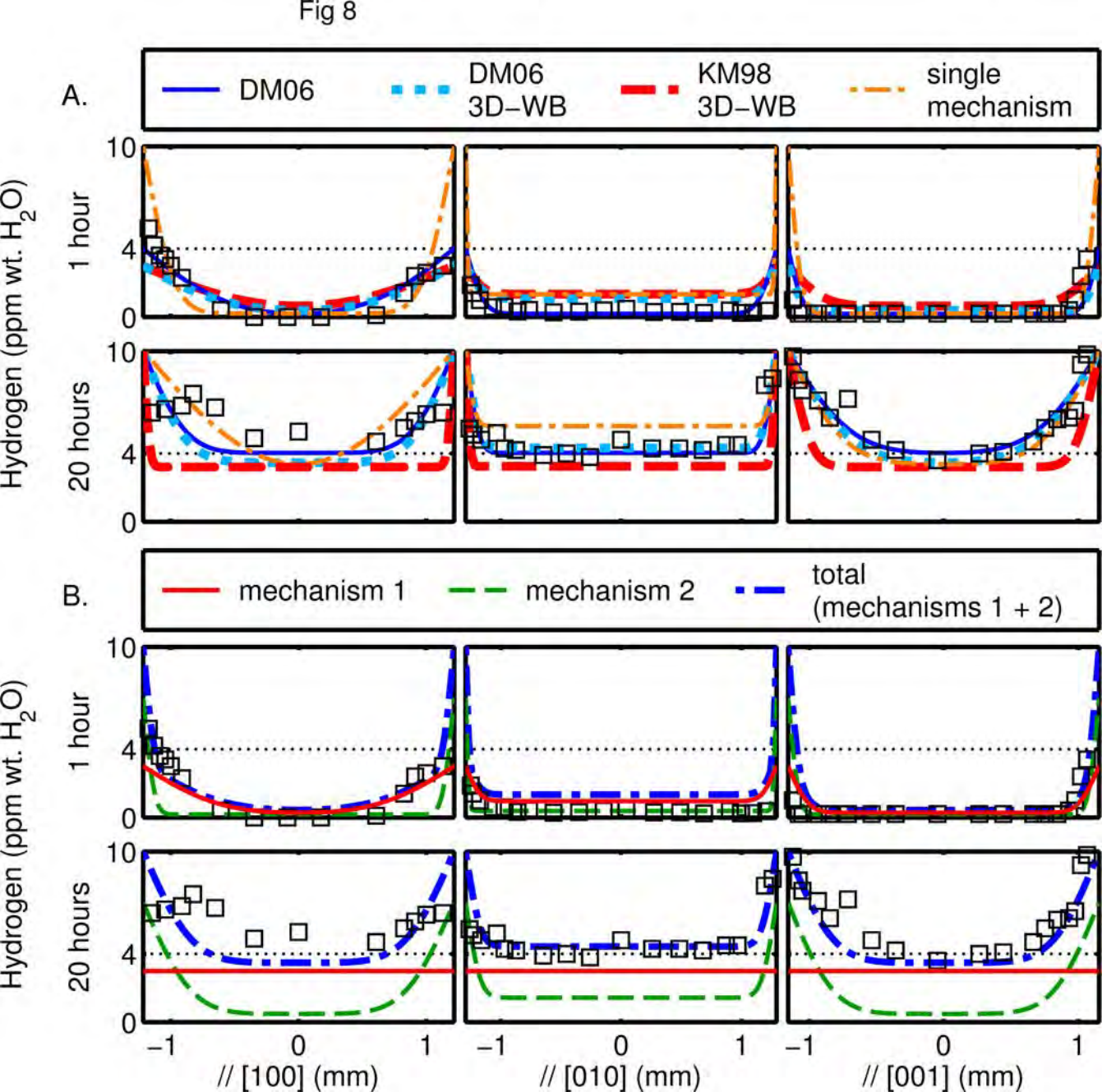
A.
DM06
DM06 3D−WB
KM98 3D−WB
single mechanism
1 hour
20 hours
Hydrogen (ppm wt. H_2O)
B.
mechanism 1
mechanism 2
total (mechanisms 1 + 2)
1 hour
20 hours
Hydrogen (ppm wt. H_2O)
10
4
0
−1
0
1
// [100] (mm)
// [010] (mm)
// [001] (mm)

Fig 9

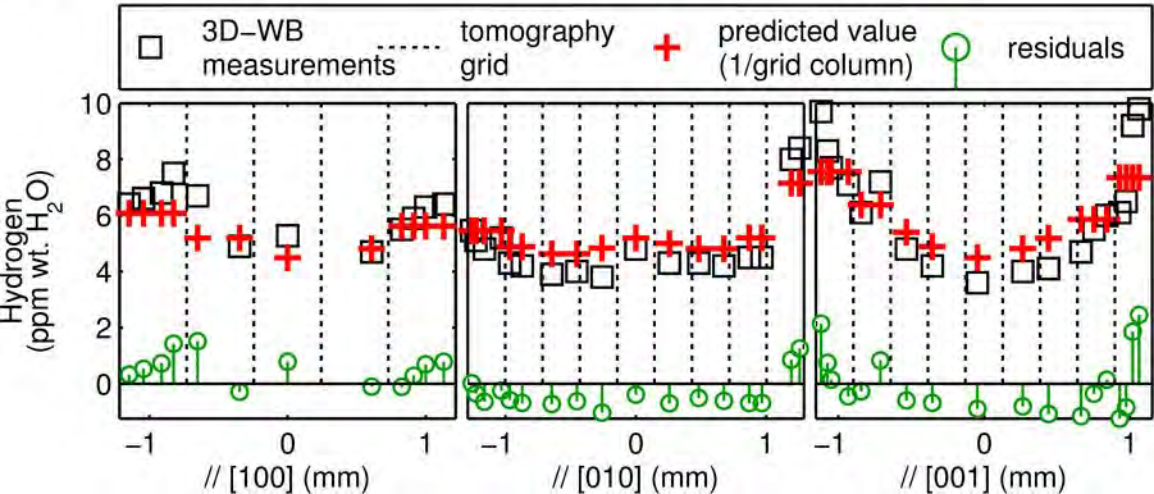
3D–WB measurements
tomography grid
predicted value (1/grid column)
residuals
Hydrogen (ppm wt. H_2O)
10
8
6
4
2
0
–1
0
1
// [100] (mm)
// [010] (mm)
// [001] (mm)

Fig 10

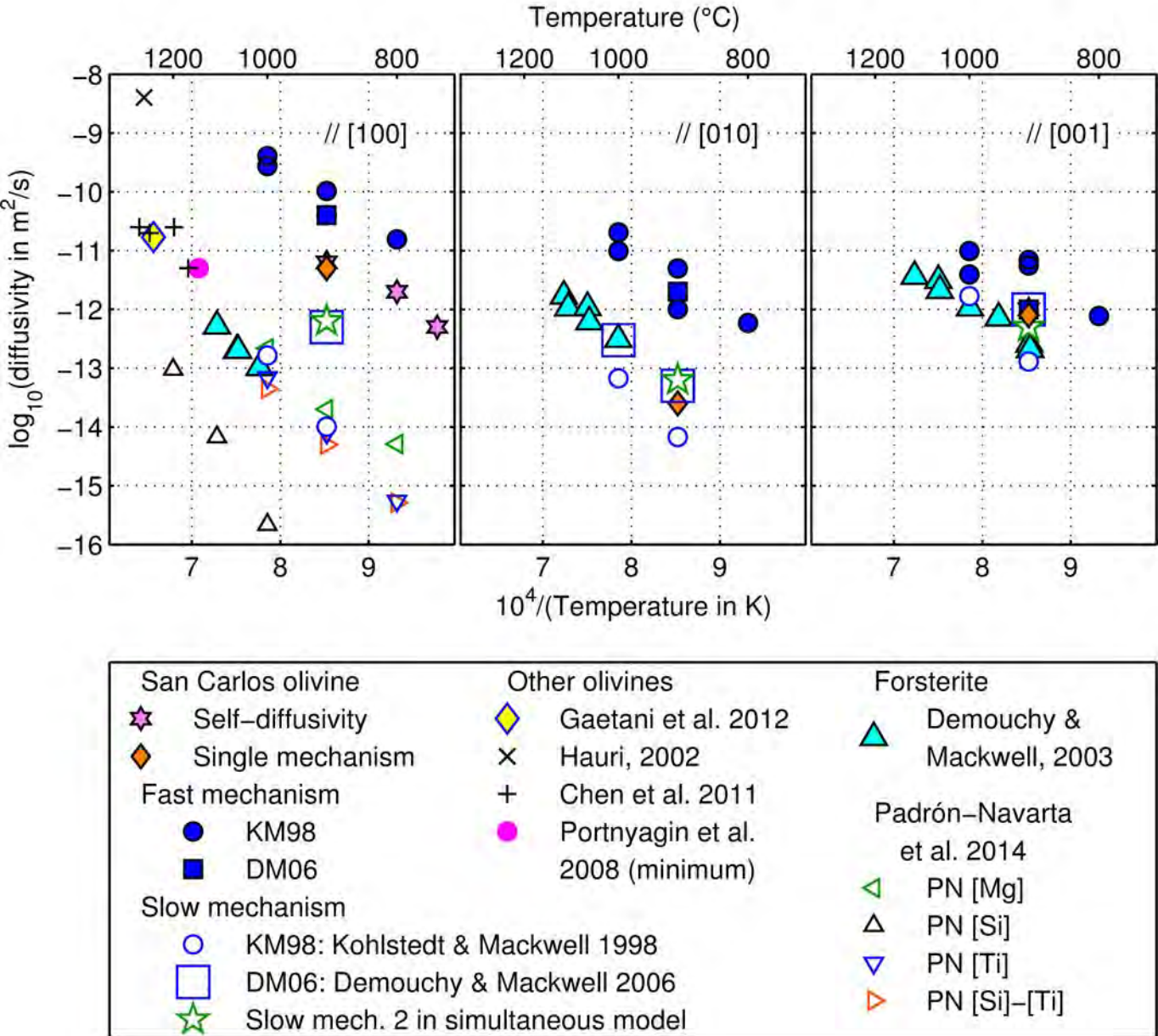
Temperature (°C)
1200
1000
800
−8
−9
−10
−11
−12
−13
−14
−15
−16
// [100]
// [010]
// [001]
log10(diffusivity in m2/s)
7
8
9
10^4/(Temperature in K)
San Carlos olivine
Self−diffusivity
Single mechanism
Fast mechanism
KM98
DM06
Slow mechanism
KM98: Kohlstedt & Mackwell 1998
DM06: Demouchy & Mackwell 2006
Slow mech. 2 in simultaneous model
Other olivines
Gaetani et al. 2012
Hauri, 2002
Chen et al. 2011
Portnyagin et al. 2008 (minimum)
Forsterite
Demouchy & Mackwell, 2003
Padrón−Navarta et al. 2014
PN [Mg]
PN [Si]
PN [Ti]
PN [Si]−[Ti]

grid // [100]	grid // [010]	grid // [001]	λ	σ^2	concentation at the center (ppm wt. H2O)
1	1	1	0.05	3.7	5.8
2	2	2	0.05	0.4	4.4
3	3	3	0.05	0.08	3.6
5	5	5	0.05	0.01	2.9
5	7	7	0.05	0.005	2.9
5	9	9	0.05	0.002	2.9
5	11	9	0.05	0.002	2.9
5	9	9	0.2	0.003	3.2
5	9	9	0.5	0.01	5.2

Hydrogen in diopside	**$\log_{10}D$ // [100]***	**$\log_{10}D$ // [010]**	**$\log_{10}D$ // [001]**	**r^2**
3D-WB fit to 3D-WB FTIR measurements	-13.0±0.2	-13.4±0.2	-13.6±0.3	0.64
3D-NPI fit to 3D-WB FTIR measurements	-12.8±0.3	-13.7±0.3	-12.4±0.1	0.21
3D-NPI fit to slice FTIR measurements	N/A	-13.1±0.3	-13.1±0.2	0.87 // [010] 0.76 // [001]
3D-NPI fit to slice SIMS measurements	N/A	-13.3±0.4	-13.2±0.4	0.90 // [010] 0.76 // [001]

Fitting approach	Geometry of measurements	Measurements used in fit (experimental time in hours)	Diffusion mechanism	Initial concentration used in fit (ppm wt. H2O)	Solubility used in fit (ppm wt. H2O)	logD // [100]
1D	Slice	1	fast	0	1.8*	-10.2
		8	slow	0.4*	3*	-14.0
3D-NPI	3D-WB	1	fast	0	4	-10.4
		20	slow	4	10	-12.3
3D-WB	3D-WB	1	fast	0	3	-10.2
		20	slow	3	10	-14.0
3D-WB	3D-WB	1	fast	0	3	-10.4
		20	slow	3	10	-12.3
3D-WB	3D-WB	1 and 20	fast	0	3	-10.2
		1 and 20	slow	0	7	-12.2±0.3
3D-WB	3D-WB	1 and 20	single	0	10	-11.3±0.1

*Kohlstedt and Mackwell 1998 use a different calibration scheme than Demouchy and Mackwell 2006 and report their concentrations in H / 10^6 Si, wh

logD // [010]	logD // [001]	r2 for fits to both 1 hr and 20 hr 3D-WB measurements of Demouchy and Mackwell 2006	Reference
-11.7 -14.2	-11.2 -12.9	N/A	Kohlstedt and Mackwell (1998) (KM98)
-11.7 -13.3	-12.0 -12.0	0.89	Demouchy and Mackwell (2006) (DM06)
-11.7 -14.2	-11.2 -12.9	0.61	This study: 3D-WB applied using KM98
-11.7 -13.3	-12.0 -12.0	0.87	This study: 3D-WB applied using DM06
-11.7 -13.2±0.5	-11.2 -12.3±0.3	0.83	This study: Simultaneous fit assuming KM98 fast mechanism
-13.6±0.6	-12.1±0.2	0.79	This study: Single mechanism

ıich we convert to ppm wt. H2O by dividing by 16.3

	Position // [100]* (mm)	Hydrogen // [100]* (ppm wt. H2O)	Position // [010] (mm)	Hydrogen // [010] (ppm wt. H2O)	Position // [001] (mm)
3D-WB FTIR measurements	-1.68	8.8	-0.75	9.0	-0.83
	-1.58	15.2	-0.65	20.7	-0.73
	-1.43	21.2	-0.50	27.5	-0.58
	-1.33	24.5	-0.40	26.8	-0.48
	-1.23	25.1	-0.30	28.9	-0.38
	-1.13	24.8	-0.20	31.8	-0.28
	-1.03	25.5	-0.10	31.1	-0.18
	-0.83	25.2	0.00	33.3	-0.08
	-0.63	26.4	0.10	31.9	0.02
	-0.33	26.2	0.20	31.4	0.12
	0.08	28.9	0.30	31.4	0.22
	0.38	28.2	0.40	29.9	0.32
	0.68	26.0	0.50	29.9	0.42
	0.78	27.0	0.60	30.5	0.52
	0.88	27.8	0.65	27.0	0.62
	0.98	28.3	0.75	20.0	0.72
	1.08	27.2			
	1.18	26.7			
	1.28	28.1			
	1.38	30.0			
Slice FTIR measurements	N/A	N/A	-0.75	1.0	-0.83
			-0.66	14.5	-0.73
			-0.51	26.6	-0.63
			-0.41	25.6	-0.53
			-0.21	32.2	-0.43
			-0.01	28.2	-0.33
			0.19	33.1	-0.23
			0.49	35.1	-0.13
			0.59	28.9	-0.03
			0.69	16.1	0.07

			0.79	10.3	0.17 0.27 0.37 0.47 0.63 0.73 0.83
Slice SIMS measurements	N/A	N/A	-0.75 -0.66 -0.51 -0.41 -0.31 -0.21 -0.11 0.09 0.19 0.29 0.39 0.49 0.59 0.69 0.79	3.8 25.0 31.8 33.7 33.4 34.7 35.5 34.1 44.9 34.5 34.5 34.2 29.6 7.8 3.4	-0.83 -0.73 -0.63 -0.53 -0.43 -0.33 -0.23 -0.03 0.07 0.17 0.27 0.37 0.47 0.63 0.73 0.83

Hydrogen // [001] (ppm wt. H2O)
15.8
20.9
24.9
25.9
27.8
27.7
28.8
28.7
29.0
28.8
29.1
27.9
27.4
25.8
24.5
18.1
6.6
12.5
20.0
27.7
32.8
33.0
34.0
33.9
28.2
29.0

28.8
29.4
31.0
30.2
30.2
24.8
13.6
5.6
12.9
31.3
35.1
34.2
29.7
32.3
29.7
25.9
25.3
25.4
24.9
25.5
30.9
25.6
6.6